# Generalized longitudinal strong focusing in a steady-state microbunching storage ring

Zizheng Li,[1] Xiujie Deng,[1] Zhilong Pan,[1] Chuanxiang Tang,[1,*] and Alexander Chao[2,3,†]

[1]*Department of Engineering Physics, Tsinghua University, Beijing 100084, China*
[2]*Institute for Advanced Study, Tsinghua University, Beijing 100084, China*
[3]*Stanford University, Stanford, California 94309, USA*

(Received 25 May 2023; accepted 23 October 2023; published 13 November 2023)

Steady-state microbunching (SSMB) storage rings are an appealing option for high-power extreme ultraviolet (EUV) light sources. In this paper, we propose a generalized longitudinal strong focusing (GLSF) scheme to boost the average power of short-wavelength radiation from an SSMB source with a technical demand within the present reach. This scheme employs transverse-longitudinal coupling dynamics to produce steady-state ultrashort bunches and reduces the required modulation laser power significantly by exploiting the low vertical beam emittance in a planar ring. Linear beam dynamics are studied in detail, including bunch compression, modulation cancellation, and vertical-longitudinal decoupling. An instance of a linear lattice layout is given, and kW-level quasicontinuous-wave 13.5-nm EUV radiation can be achieved in a GLSF SSMB storage ring with 1-MW modulation laser power. We believe that the GLSF scheme can also be used in conventional storage rings for various purposes concerning beam manipulation.

DOI: 10.1103/PhysRevAccelBeams.26.110701

## I. INTRODUCTION

The reduction of light wavelength in lithography plays a crucial role in minimizing the feature size of integrated circuit designs, bringing about significant breakthroughs in computer chip fabrication [1]. Throughout its evolution from 436, 365, 248, and 193 nm, the cutting-edge wavelength resides at 13.5 nm within the extreme ultraviolet (EUV) range. The industry is eagerly seeking light sources capable of delivering EUV radiation of over 1 kW to enable high-volume microchip manufacturing. While ASML-delivered systems have achieved a power of 330 W [2], exploring the potential of accelerator-based light sources still holds great promise for producing high-power EUV radiation.

The power of radiation from an accelerator source relies on the coherence and repetition rate of the radiation. These factors can be effectively enhanced through a cost-effective method called steady-state microbunching (SSMB) [3], which allows for the emergence and stable maintenance of microbunching in a storage ring. Laser modulators consisting of lasers and undulators are employed to achieve bunching, instead of radio-frequency (rf) cavities typically utilized in conventional rings. By reducing the modulation wavelength by 6 orders of magnitude, the equilibrium bunch length is decreased substantially, enabling the generation of coherent short-wavelength radiation. It should be noted that the undulator used in SSMB is relatively short and does not involve a free-electron-laser (FEL) mechanism. As a result, the beam remains almost intact and can radiate at high repetition rates on a turn-by-turn basis.

As an appealing option for high-power EUV sources, SSMB has made notable progress in recent years [4–11]. One of the key areas of research focuses on addressing the gap between the bunch length attainable (a few tens of nanometers, as illustrated in the next section) in the SSMB storage ring and that required (a few nanometers) for generating coherent 13.5-nm EUV radiation, as shown in Fig. 1.

Scenarios have been proposed to achieve further compression of bunches to nanometer scale within the radiation section, including longitudinal weak focusing (LWF) and longitudinal strong focusing (LSF) [4]. It should be noted that the ultrashort bunch length at the radiator should be an eigenstate and can be achieved repeatedly, distinguishing it from bunch compression schemes used in single-pass devices.

This paper proposes a generalized longitudinal strong focusing (GLSF) scheme. GLSF incorporates transverse-longitudinal coupling, inspired by previous works [12–14], and exploits the intrinsic low vertical emittance in a planar horizontal-vertical-uncoupled storage ring. By implementing the GLSF scheme in an SSMB storage ring, it is

*tang.xuh@tsinghua.edu.cn
†achao@slac.stanford.edu

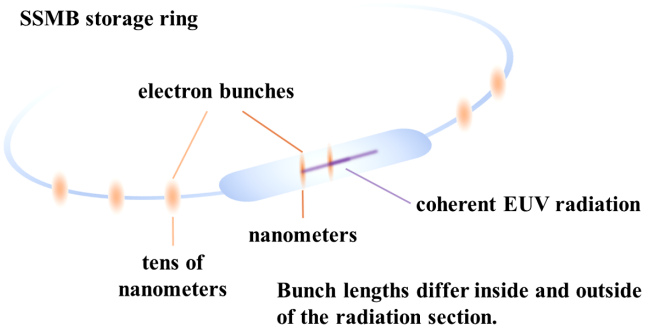


FIG. 1. Diagram showing the gap between the bunch length attainable (tens of nanometers) in the SSMB ring and that required (nanometers) for coherent 13.5-nm EUV radiation.

expected that a steady-state bunch length of 3 nm can be achieved at the radiator, enabling the generation of kW-level quasi-continuous-wave 13.5-nm EUV radiation. The required modulation laser power is estimated to be 1 MW, which is a challenging but realizable value using optical cavities operating in continuous-wave mode.

The paper is structured as follows: First, we introduce the generalized longitudinal strong focusing scheme and highlight its distinctions from the existing longitudinal weak focusing and longitudinal strong focusing schemes. Then, we delve into bunch compression schemes tailored for storage rings based on transverse-longitudinal coupling. We propose a general lattice layout and two specific types: symmetric and reversible. Moving forward, we investigate the linear beam dynamics involved in the GLSF scheme, including bunch compression, modulation cancellation, and transverse-longitudinal decoupling. In addition, we provide an exploration of the strategies employed to realize a practical linear lattice for GLSF, presenting the parameters and performance of one example linear lattice. Finally, we briefly discuss relevant topics such as the nonlinear dynamics.

## II. GENERALIZED LONGITUDINAL STRONG FOCUSING

In this section, schemes to achieve a steady-state bunch length of 3-nm level in storage rings are inspected. Before diving into generalized longitudinal strong focusing, two existing schemes (longitudinal weak focusing and longitudinal strong focusing) are reviewed first.

### A. Longitudinal weak focusing (LWF)

In conventional storage rings equipped with an rf cavity, the equilibrium bunch length given by Sands [15] is as follows:

$$\sigma_s = \sigma_\delta \beta_s C_0 \sqrt{-\frac{E_s}{2\pi e V_0 \cos(\phi_s)} \frac{\eta}{h_r}}, \tag{1}$$

where $\sigma_\delta$ represents the natural energy spread, $\beta_s$ is the ratio of the speed of the synchronous particle to the speed of light, $C_0$ denotes the ring circumference, $E_s$ stands for the energy of the synchronous particle, $e$ represents the elementary charge, $V_0$ represents the rf voltage, $\phi_s$ represents the synchronous phase, $\eta$ represents the ring phase slippage factor, and $h_r$ represents the rf harmonic number. The rf harmonic number is defined as the ratio of the rf (modulation) frequency $\omega_{rf}$ to the revolution frequency $\omega_0$ at which a synchronous particle revolves. In other words, $h_r = \frac{\omega_{rf}}{\omega_0}$.

Please note that the diffusion of particle longitudinal position can also arise from the stochastic nature of the location where photon emission occurs. It can be quantified by a parameter called local phase slippage [16–18]. Although this effect is typically not dominant in conventional rings, it should be treated with caution when attempting to further reduce the bunch length.

The equilibrium bunch length in conventional rings is approximately 6 orders of magnitude larger than the desired value for coherent EUV radiation. Although certain parameters such as $E_s$, $\sigma_\delta$, $C_0$, and $V_0$ are relatively constrained, reducing the value of $\eta/h_r$ can be an effective approach to decrease the bunch length.

In an SSMB ring, a typical choice of phase slippage factor is $\eta = 5 \times 10^{-7}$, which is relatively small but still feasible. The rf cavity is replaced by a laser modulator with a wavelength of $\lambda_m = 1$ μm. Other parameters are set as follows: $E_s = 400$ MeV, $\sigma_\delta = 2.5 \times 10^{-4}$, $C_0 = 150$ m, and $V_0 = 250$ kV (corresponding to 1-MW laser power). It is worth noting that efforts are made to control and minimize bunch lengthening resulting from local phase slippage, ensuring that it remains nondominant [19]. Consequently, the equilibrium bunch length along the ring is approximately 40 nm.

Achieving a bunch as short as 3 nm would require further reducing $\eta/h_r$ by 2 orders of magnitude, which is beyond the current state-of-the-art feasibility.

The cases discussed above can be categorized into longitudinal weak focusing rings as shown in Fig. 2.

In contrast to the longitudinal strong focusing cases discussed later, the longitudinal weak focusing cases exhibit a synchrotron tune ($\nu_s$) that is significantly smaller than 1 ($\nu_s \ll 1$). The longitudinal focusing in these cases is considered "weak" due to the moderate modulation and the absence of strong variations in the bunch length along the ring. The evolution of the position-dependent longitudinal beta function [20] ($\beta_z$), which is an indicator of the bunch length ($\sigma_z(s) = \sqrt{\epsilon_z \beta_z(s)}$ where $\epsilon_z$ is the longitudinal emittance), is relatively insignificant. In other words, the longitudinal alpha function $\alpha_z$ along the ring is close to 0.

In an LWF ring, the laser modulator, labeled as Mod0 in Fig. 2, fulfills a function comparable to that of an rf cavity in a conventional ring. It establishes for electrons a stable region within the longitudinal dimensions.

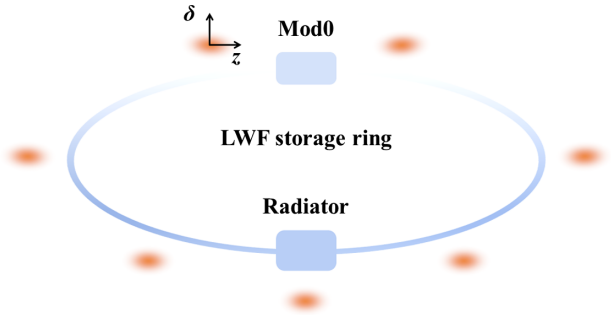


FIG. 2. Diagram showing the components of a longitudinal weak focusing (LWF) ring with one laser modulator (Mod0). Ovals in orange show the beam distribution evolution in the longitudinal phase space.

This region, similar to the concept of an "rf bucket," could be referred to as the "laser-bucket' in the context of SSMB beam dynamics.

### B. Longitudinal strong focusing (LSF)

The concept of longitudinal strong focusing has then been introduced [4,21]. In this approach, instead of using one single component with moderate strength, multiple intensified laser modulators are incorporated into the ring to serve as the longitudinal focusing and defocusing elements, analogous to the role of quadrupoles in transverse focusing. The momentum compaction factor, denoted as $r_{56}$, is considered as the longitudinal equivalent of a drift space. It should be noted that $r_{56}$ can have either a positive or negative value. Due to the significantly stronger modulation strength, the synchrotron tune can now be comparable to or even greater than 1.

An example showing an LSF ring with two modulation modules in the radiation section is sketched in Fig. 3.

It is possible to generate the desired short bunches for radiation $[\sigma_z(\mathrm{Rad}) = \sqrt{\epsilon_z \beta_z(\mathrm{Rad})}]$ by reducing the longitudinal emittance $\epsilon_z$ and the beta function at the radiator $\beta_z(\mathrm{Rad})$. Unlike in LWF rings, the beta function

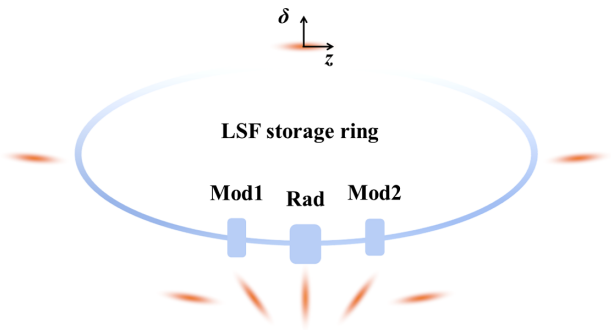


FIG. 3. Diagram showing the components of a longitudinal strong focusing (LSF) ring with two laser modulators (Mod1, Mod2). Ovals in orange show the beam distribution evolution in the longitudinal phase space.

$\beta_z$ and equilibrium bunch length $\sigma_z$ undergo significant changes throughout the ring. This means that the bunch length at other locations in the ring may not be as short as that at the radiator.

An example of an LSF ring is illustrated [21]. In this particular case, two laser modulators are used to suppress the beta function in the radiator. The bunch length at the radiator is $\sigma_z(\mathrm{Rad}) = 2$ nm, while at the opposite location to the radiator around the storage ring, it is $\sigma_z(\mathrm{R}_0) = 28$ nm. The bunch length compaction factor, defined as $R_c = \frac{\sigma_z(\mathrm{R}_0)}{\sigma_z(\mathrm{Rad})}$, is 14. Notably, the bunch length experiences significant variation when passing through the radiation section.

Achieving a short bunch using the LSF approach comes with, unfortunately, the tradeoff of increased modulation strengths, which leads to higher laser power requirements. In this specific case [21], a power of 300 MW is demanded for a 1-μm laser. However, the power of modulation lasers in continuous-wave mode is limited to the MW level by state-of-the-art technology. This limitation poses a challenge for the LSF scheme to generate kW-level average power of EUV radiation in storage rings, as the optical cavity can only operate in pulsed mode.

### C. Generalized longitudinal strong focusing (GLSF)

A generalized longitudinal strong focusing (GLSF) approach is proposed to relieve the demand for modulation laser power by involving transverse-longitudinal coupling dynamics and exploiting the low vertical emittance in a planar horizontal-vertical-uncoupled ring.

A vital distinction between the LWF and LSF schemes lies in the nature of the manipulation in the longitudinal phase space. The manipulation is mild in weak focusing cases and becomes more intense in strong focusing cases, as illustrated in Figs. 2 and 3. The strong manipulation in the longitudinal phase space often leads to significant variations in the bunch length, thereby enabling the generation of ultrashort bunches.

The GLSF scheme builds upon the spirit of the LSF approach, which involves bunch compression through phase space manipulation. The number of dimensions included in GLSF manipulation, however, has been expanded from two (longitudinal alone) to four (transverse-longitudinal coupled) or even six.

The reason for considering transverse-longitudinal coupling dynamics can be clarified as follows: Bunch length can be seen as the projection of eigenemittances onto the coordinate $z$ in phase space. Therefore, it is preferable to project the eigenemittance with the smallest value in order to reduce the bunch length. In a planar ring, for instance, among the three eigenemittances of the uncoupled beam $(\epsilon_x, \epsilon_y, \epsilon_z)$, $\epsilon_y$ is relatively small compared to $\epsilon_z$ and $\epsilon_x$. By introducing vertical-longitudinal coupling and carefully manipulating the beam, the bunch length at the radiator

can be expressed as $\sigma_z(\mathrm{Rad}) \propto \sqrt{\epsilon_y}$ instead of $\sigma_z(\mathrm{Rad}) \propto \sqrt{\epsilon_z}$. As a result, the required modulation strength in the GLSF approach can be significantly reduced compared to the LSF scheme. Additionally, this reduction in modulation strength leads to a decrease in the laser power requirement, as the power of the modulation laser, denoted as $P_{\mathrm{laser}}$, is proportional to the square of the modulation strength, represented by $h$, i.e., $P_{\mathrm{laser}} \propto h^2$. Assuming $\epsilon_y = 1$ pmrad, the GLSF scheme only requires a modulation laser power of 1 MW or lower to generate a 3-nm bunch. By operating at such a low power level in comparison to the LSF scheme, it becomes feasible to achieve quasicontinuous generation of EUV radiation, which in turn allows for an increase in the average radiation power. Hence, this is the motive we explore the application of the GLSF approach in SSMB storage rings in this paper.

It is worth noting that in general both $\epsilon_z$ and $\epsilon_y$ contribute to bunch length $\sigma_z$ in most regions where vertical-longitudinal coupling is present. The exclusive reliance of $\sigma_z$ on $\epsilon_y$ at the radiator, however, is a unique case resulting from deliberate lattice design. On the other hand, the GLSF approach is not subject to the concept of double emittance exchange. At the center of the radiator, while the vertical emittance $\epsilon_y$ alone shapes the bunch length, coupling effects can still affect other beam parameters, including bunch size, divergence, and energy spread, as illustrated in the subsequent sections.

In practice, the laser modulator is typically positioned at a dispersive location to intentionally introduce the desired transverse-longitudinal coupling. However, in order to preserve a small transverse eigenemittance, which is essential for the success of the GLSF approach, it is necessary to eliminate the coupling between the transverse and longitudinal dimensions once the coherent radiation has been produced.

GLSF can be realized through various approaches. An example showing a GLSF ring with two laser modulators in the radiation section is sketched in Fig. 4.

The storage ring depicted in Fig. 4 has been designed for operation under LWF conditions, where the beam distribution in the longitudinal phase space does not vary much throughout the ring (except in the radiation section). In this setup, a laser modulator (Mod0) is employed to create stable regions for electrons and prebunch the beam, as explained in Sec. II A. Since Mod0 has a weak modulation strength and the longitudinal alpha function ($\alpha_z$) is negligible, the energy chirps at the entrance and exit of the radiation section are disregarded. While the laser-prebunched beams have the potential to enhance the output radiation power, it is important to emphasize that the GLSF approach is also capable of accommodating rf-prebunched or coasting beams.

In the radiation section, the bunch length exhibits noticeable variations. Neglecting the influences of radiation damping and quantum diffusion, it is important to note that

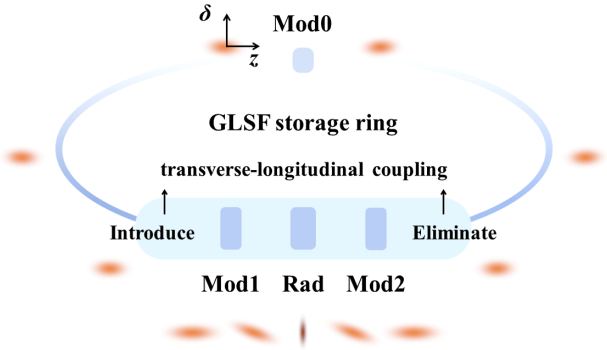


FIG. 4. Diagram showing the components of a generalized longitudinal strong focusing (GLSF) ring with two laser modulators (Mod1, Mod2) in the radiation section and one in the ring (Mod0). Transverse-longitudinal coupling is intentionally introduced at the entrance of the radiation section and subsequently eliminated at the exit of the radiation section. Beam distribution evolution in the longitudinal phase space is sketched in orange ovals.

the overall 6D phase space volume of the beam remains conserved according to Liouville's theorem [20]. However, the projected phase space area in the longitudinal plane can vary and is not necessarily constant along the trajectories. It is possible to achieve a short bunch length at the radiator without a significant increase in energy spread. This characteristic distinguishes the GLSF approach and highlights one of its differences from LSF rings.

Now a brief comparison can be made among the three schemes discussed above.

(i) LWF: minor variation in the bunch length within the storage ring; manipulation in the longitudinal phase space. (ii) LSF: notable variation in the bunch length within the storage ring; manipulation in the longitudinal phase space. (iii) GLSF: notable variation in the bunch length within the radiation section, while minor variation in the ring; manipulation in the transverse-longitudinal-coupled phase space.

Several transverse-longitudinal coupling schemes have been proposed for high harmonic generation in FELs. Some of these schemes involve the use of deflecting rf cavities or $\mathrm{TEM}_{01}$ mode lasers [12,22–24], as well as wave-front tilted seed lasers or dual-tilted-laser modulation [25–28]. However, these approaches may not be the most suitable choices for an SSMB storage ring due to their high requirements, especially when aiming for a low modulation laser power of 1 MW [29]. On the other hand, schemes based on normal rfs or $\mathrm{TEM}_{00}$ mode lasers are still feasible even with 1-MW modulation lasers [30]. These include phase-merging enhanced harmonic generation (PEHG) [13,31–33] and angular dispersion-induced microbunching (ADM) [14,34–36]. They have provided inspiration for achieving the desired transverse-longitudinal coupling in an SSMB storage ring.

In the PEHG and ADM schemes, the relationship between the final bunch length ($\sigma_{z\mathrm{f}}$) and the initial vertical beam parameters can be expressed as $\sigma_{z\mathrm{f}}^{\mathrm{PEHG}} \propto \sigma_{y\mathrm{i}}$ and $\sigma_{z\mathrm{f}}^{\mathrm{ADM}} \propto \sigma_{y'\mathrm{i}}$, where $\sigma_{y\mathrm{i}}$ and $\sigma_{y'\mathrm{i}}$ represent the initial vertical beam size and divergence, respectively. Meanwhile, the compressed bunch length in the GLSF scheme is derived from the projection of the vertical eigenemittance $\epsilon_y$ of the beam and is therefore proportional to $\sqrt{\epsilon_y}$. Thus, PEHG and ADM can be seen as specific scenarios that fit within the overarching category of the GLSF scheme. It is important to note that, unlike PEHG and ADM, the GLSF approach goes beyond single-pass bunch compression. Instead, it aims to provide a steady-state eigensolution applicable to storage rings. The intricate beam dynamics involved, including the mechanisms for debunching, decoupling, and returning of the beam into the storage ring to achieve steady-state microbunching, will be explored in the subsequent sections.

## III. VERTICAL-LONGITUDINAL COUPLING SCHEMES FOR GLSF

The vertical-longitudinal coupling case is analyzed as an example, considering the typically low vertical emittance. In this section, two categories of lattice layouts are proposed, specifically designed as insertion units within storage rings. These layouts aim to facilitate the bunching and debunching process on a turn-by-turn basis.

### A. Vertical-longitudinal coupling schemes

To start with, a bunch compression unit manipulating the longitudinal dimensions alone is presented. This unit can be broken down into two functional features: (i) an energy chirp ($h$) to correlate $\delta$ with $z$, and (ii) momentum compaction ($\xi$) to correlate $z$ with $\delta$.

Here $\delta$ and $z$ are the energy deviation and longitudinal displacement relative to the synchronous particle. A matrix analysis may help to explain:

$$\mathbf{M_i} = \begin{pmatrix} 1 & 0 \\ h & 1 \end{pmatrix}, \qquad \mathbf{M_{ii}} = \begin{pmatrix} 1 & \xi \\ 0 & 1 \end{pmatrix}. \tag{2}$$

Here the phase space coordinates are $(z, \delta)$. $\mathbf{M_i}$ and $\mathbf{M_{ii}}$ represent the transfer matrix of the two features defined above. In $\mathbf{M_i}$, the sinusoidal modulation has been linearized around the zero-crossing phase. The transfer matrix of the bunch compression unit is then:

$$\mathbf{M_{bc}} = \mathbf{M_{ii}}\mathbf{M_i} = \begin{pmatrix} 1 + h\xi & \xi \\ h & 1 \end{pmatrix}. \tag{3}$$

By adjusting the values of $h$ and $\xi$, it is possible to make the particle position at the end of the unit, denoted as $z_{\mathrm{f}}$, independent of its position at the entrance, represented as $z_{\mathrm{i}}$. And when the condition $1 + h\xi = 0$ is satisfied, it follows that $\sigma_{z\mathrm{f}} = |\xi|\sigma_{\delta\mathrm{i}} = \sigma_{\delta\mathrm{i}}/|h|$. However, a significant modulation strength $|h|$ is still needed to mitigate the bunch length contribution stemming from the initial energy spread $\sigma_{\delta\mathrm{i}}$. As a result, generating 3-nm bunches with SSMB parameter sets would require a modulation laser power of approximately 300 MW.

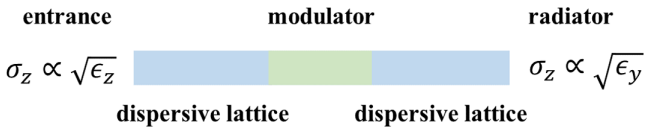


FIG. 5. Schematic layout of a bunch compression scheme based on vertical-longitudinal coupling.

It is possible to remove the impact of $\delta_{\mathrm{i}}$ on $z_{\mathrm{f}}$. A bunch compression scheme employing vertical-longitudinal coupling is depicted in Fig. 5.

In this scheme, two dispersive components are incorporated. This layout can be broken down into four functional features: (i) dispersion ($r_{36} = D_1$ and $r_{46} = D_1'$) to correlate $y$ and $y'$ with $\delta$, (ii) an energy chirp ($r_{65} = h$), (iii) momentum compaction ($r_{56} = \xi$), and (iv) dispersion ($r_{53} = -D_2'$ and $r_{54} = D_2$) to correlate $z$ with $y$ and $y'$.

In this setup, the initial energy spread $\delta_{\mathrm{i}}$ is converted into $y$ and $y'$ as the beam passes through component (i). Subsequently, through the coupling provided by component (iv), it is converted back to $z$. This additional contribution to $z_{\mathrm{f}}$ arising from $\delta_{\mathrm{i}}$ can be adjusted to effectively cancel out the term $z_{\mathrm{f}} = \xi\delta_{\mathrm{i}}$. A matrix analysis may help to explain:

$$\mathbf{M_1} = \begin{pmatrix} 1 & 0 & 0 & D_1 \\ 0 & 1 & 0 & D_1' \\ -D_1' & D_1 & 1 & 0 \\ 0 & 0 & 0 & 1 \end{pmatrix}, \quad \mathbf{M_2} = \begin{pmatrix} 1 & 0 & 0 & 0 \\ 0 & 1 & 0 & 0 \\ 0 & 0 & 1 & 0 \\ 0 & 0 & h & 1 \end{pmatrix},$$
$$\mathbf{M_3} = \begin{pmatrix} 1 & 0 & 0 & 0 \\ 0 & 1 & 0 & 0 \\ 0 & 0 & 1 & \xi \\ 0 & 0 & 0 & 1 \end{pmatrix}, \quad \mathbf{M_4} = \begin{pmatrix} 1 & 0 & 0 & D_2 \\ 0 & 1 & 0 & D_2' \\ -D_2' & D_2 & 1 & 0 \\ 0 & 0 & 0 & 1 \end{pmatrix}. \tag{4}$$

In this context, the phase space coordinates are denoted as $(y, y', z, \delta)$. The transfer matrices for the four features defined above are represented as $\mathbf{M_1}$, $\mathbf{M_2}$, $\mathbf{M_3}$, and $\mathbf{M_4}$. It is important to note that the matrices are presented in their simplest form, including only relevant elements and fundamental relations like the symplectic conditions [20]. The transfer matrix for a vertical-longitudinal coupling bunch compression unit can be expressed as follows:

$$\mathbf{M_{bc0}} = \mathbf{M_4 M_3 M_2 M_1} = \begin{pmatrix} 1 - hD_1' D_2 & hD_1 D_2 & hD_2 & D_1 + D_2, \\ -hD_1' D_2' & 1 + hD_1 D_2' & hD_2' & D_1' + D_2'. \\ -D_2' - D_1'(1 + h\xi) & D_2 + D_1(1 + h\xi) & 1 + h\xi & D_1' D_2 - D_1 D_2' + \xi \\ -hD_1' & hD_1 & h & 1 \end{pmatrix}. \tag{5}$$

The bunch compression conditions are then:

$$\begin{aligned} 1 + h\xi &= 0 \\ D_1' D_2 - D_1 D_2' + \xi &= 0. \end{aligned} \tag{6}$$

As discussed above, the contributions to $z_f$ from vertical-longitudinal coupling, $(D_1' D_2 - D_1 D_2')\delta_i$, and from momentum compaction, $\xi\delta_i$, can now cancel each other. Applying Eq. (6), there is:

$$z_f = -D_2' y_i + D_2 y_i'. \tag{7}$$

Here $(y_i, y_i')$ represents the initial vertical position and slope. In the scenario where the beam at the entrance of the unit is assumed to be decoupled in the vertical and longitudinal dimensions and follows a Gaussian distribution, the matrix representing the second-order moments of the beam takes the form:

$$\mathbf{\Sigma_i} = \begin{pmatrix} \epsilon_y \beta_{yi} & -\epsilon_y \alpha_{yi} & 0 & 0 \\ -\epsilon_y \alpha_{yi} & \epsilon_y \gamma_{yi} & 0 & 0 \\ 0 & 0 & \epsilon_z \beta_{zi} & -\epsilon_z \alpha_{zi} \\ 0 & 0 & -\epsilon_z \alpha_{zi} & \epsilon_z \gamma_{zi} \end{pmatrix}. \tag{8}$$

In this context, $\epsilon_y$ and $\epsilon_z$ represent the eigenemittances of the beam, which are invariant quantities in a linear symplectic lattice. $(\alpha, \beta, \gamma)$ correspond to the Courant-Snyder functions. Then the bunch length at the exit of the bunch compression unit is expressed as follows:

$$\sigma_{zf} = \sqrt{\epsilon_y (D_2'^2 \beta_{yi} + 2 D_2 D_2' \alpha_{yi} + D_2^2 \gamma_{yi})} = \sqrt{\epsilon_y \mathcal{H}_y}. \tag{9}$$

In this vertical-longitudinal coupling scheme, the generated bunch length at the exit is determined solely by the vertical emittance, as opposed to the longitudinal emittance. The contribution from the vertical emittance to the bunch lengthening is quantified by the $\mathcal{H}_y$ function, which will be explained in the subsequent section.

As clarified in Sec. II C, the PEHG and ADM schemes can be regarded as specific instances of the above general relations. In the case of PEHG, in addition to Eq. (6), the conditions $D_1' = 0$ and $D_2 = 0$ need to be satisfied. This leads to the expression $\sigma_{zf}^{\mathrm{PEHG}} = \sqrt{\epsilon_y D_2'^2 \beta_{yi}} = |D_2'| \sigma_{yi}$. Meanwhile, in the ADM scheme, the extra requirements are $D_1 = 0$ and $D_2' = 0$. Consequently, the bunch length at the exit is given by $\sigma_{zf}^{\mathrm{ADM}} = \sqrt{\epsilon_y D_2^2 \gamma_{yi}} = |D_2| \sigma_{y'i}$.

In a planar horizontal-vertical-uncoupled storage ring, it is possible to achieve a vertical emittance $\epsilon_y$ as low as 1 pm rad. To generate a bunch with a length of 3 nm, a value of $\mathcal{H}_y$ of 9 μm is required. This level of $\mathcal{H}_y$ can be attained through careful lattice design and optimization.

It is important to note that at this stage, there is no explicit relationship between the bunch length and the modulation strength $h$. However, the constraint on $h$ will soon become evident when considering the degradation of the bunching factor due to the sinusoidal nonlinearity of the modulation waveform, as explained in the upcoming section. This indicates that the choice of $h$, and therefore the power of the modulation lasers, will be influenced by the desired level of bunching factor or the power of the coherent radiation to be achieved.

Up to this point, the above vertical-longitudinal coupling scheme is ready for single-pass bunch compression. However, when considering its implementation in a storage ring as an insertion unit, an important aspect to address is how to prepare the beam state as it exits the radiator to reenter the ring while maintaining a small vertical emittance. To achieve a steady-state microbunched beam at the radiator, which behaves as an eigenstate of the ring, two categories of lattice layouts are proposed as solutions in the following.

### B. Symmetric lattice layout

To debunch and decouple the beam, one strategy is to complete the beamline with a symmetric layout. The idea is that symmetry may assist the beam in reproducing its initial state at the exit. A schematic representation of a symmetric lattice layout is depicted in Fig. 6.

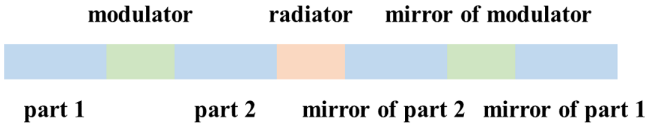


FIG. 6. Schematic layout of a symmetric lattice approach. Blue blocks are dispersive lattices. Components following the radiator are the mirror of their counterparts ahead.

Components are added as the mirror of their counterparts. The corresponding transfer matrices are as follows:

$$\mathbf{M_{4s}}=\begin{pmatrix}1 & 0 & 0 & -D_2\\ 0 & 1 & 0 & D_2'\\ -D_2' & -D_2 & 1 & 0\\ 0 & 0 & 0 & 1\end{pmatrix}\quad \mathbf{M_{3s}}=\begin{pmatrix}1 & 0 & 0 & 0\\ 0 & 1 & 0 & 0\\ 0 & 0 & 1 & \xi\\ 0 & 0 & 0 & 1\end{pmatrix}$$
$$\mathbf{M_{2s}}=\begin{pmatrix}1 & 0 & 0 & 0\\ 0 & 1 & 0 & 0\\ 0 & 0 & 1 & 0\\ 0 & 0 & h & 1\end{pmatrix}\quad \mathbf{M_{1s}}=\begin{pmatrix}1 & 0 & 0 & -D_1\\ 0 & 1 & 0 & D_1'\\ -D_1' & -D_1 & 1 & 0\\ 0 & 0 & 0 & 1\end{pmatrix}. \tag{10}$$

Here $\mathbf{M_{is}}$ is the mirror of $\mathbf{M_i}$ ($i=1,2,3,4$). The mirror of an energy chirp ($h$) or momentum compaction ($\xi$) remains the same. The transfer matrix of the symmetric lattice unit is $\mathbf{M_{sym}}=\mathbf{M_{1s}M_{2s}M_{3s}M_{4s}M_4M_3M_2M_1}$:

$$\mathbf{M_{sym}}=\begin{pmatrix}\mathbf{A} & \mathbf{B}\\ \mathbf{C} & \mathbf{E}\end{pmatrix}. \tag{11}$$

Here $\mathbf{A}$, $\mathbf{B}$, $\mathbf{C}$ and $\mathbf{E}$ are $2\times 2$ submatrices of $\mathbf{M_{sym}}$. Applying $1+h\xi=0$, there is:

$$\mathbf{B}=\begin{pmatrix}2D_1D_2D_2'h^2 & 2D_1[1+D_2'h(D_1+D_2)]\\ -2D_2'h(-1+D_2D_1'h) & -2D_2'[-1+D_1'h(D_1+D_2)]\end{pmatrix}.$$

In order to maintain a small vertical emittance, it is necessary for the beam to be initially uncoupled at the entrance of the unit and remain uncoupled at the exit. To achieve this, the submatrix $\mathbf{B}$ needs to be set to $\mathbf{0}$. This requirement implies that the following conditions should be satisfied:

$$\begin{aligned}D_1&=0,\\ D_2'&=0.\end{aligned} \tag{12}$$

The introduction of symmetry in the lattice layout cancels out certain coupling terms but also doubles the remaining terms, requiring additional constraints to be applied. By applying Eqs. (6) and (12), the total transfer matrix can be derived as follows:

$$\mathbf{M_{sym}}=\begin{pmatrix}1 & 0 & 0 & 0\\ 0 & 1 & 0 & 0\\ 0 & 0 & -1 & 2\xi\\ 0 & 0 & 0 & -1\end{pmatrix}. \tag{13}$$

Once the coupling terms have been canceled out, the beam is prepared to be reintroduced into the ring to continue its circular trajectory.

This symmetric approach is effective for a linear modulation given by $\Delta\delta=hz$. However, when a sinusoidal modulation is used, represented by $\Delta\delta=\frac{h}{k}\sin(kz)$ ($k$ is the wave number), the performance is compromised. The nonlinear terms in $z_\mathrm{f}$ and $\delta_\mathrm{f}$ at the exit of the unit can be derived:

$$\begin{aligned}z_\mathrm{f}^{\mathrm{non}}&=\frac{1}{3}k^2z_\mathrm{i}^3+o(z_\mathrm{i}^3),\\ \delta_\mathrm{f}^{\mathrm{non}}&=\frac{1}{3}k^2(hz_\mathrm{i}^3+z_\mathrm{i}^2\delta_\mathrm{i}-2\xi z_\mathrm{i}\delta_\mathrm{i}^2+4\xi^2\delta_\mathrm{i}^3)+o(z_\mathrm{i}^j\delta_\mathrm{i}^{3-j}).\end{aligned} \tag{14}$$

The clean form of Eq. (13) holds only when the modulation is perfectly linear. In cases where the modulation deviates from perfect linearity, the nonlinearities of the two modulators fail to cancel each other completely, as shown in Eq. (14). As a result, there remains a residual term that can introduce distortions in the dynamic stable region and even lead to the destruction of the steady state. This inherent nature of the symmetric lattice layout approach highlights its limitations and challenges.

### C. Reversible lattice layout

An alternative way to debunch and decouple the beam involves incorporating "reverses" after the radiator. The idea is to reverse the effects imposed on the beam so that it can restore its initial state. A schematic representation of the reversible lattice layout is depicted in Fig. 7.

Components are added as the reverse of their counterparts. The corresponding transfer matrices are as follows:

$$\mathbf{M_{4r}}=\begin{pmatrix}1 & 0 & 0 & -D_2\\ 0 & 1 & 0 & -D_2'\\ D_2' & -D_2 & 1 & 0\\ 0 & 0 & 0 & 1\end{pmatrix}\quad \mathbf{M_{3r}}=\begin{pmatrix}1 & 0 & 0 & 0\\ 0 & 1 & 0 & 0\\ 0 & 0 & 1 & -\xi\\ 0 & 0 & 0 & 1\end{pmatrix}$$
$$\mathbf{M_{2r}}=\begin{pmatrix}1 & 0 & 0 & 0\\ 0 & 1 & 0 & 0\\ 0 & 0 & 1 & 0\\ 0 & 0 & -h & 1\end{pmatrix}\quad \mathbf{M_{1r}}=\begin{pmatrix}1 & 0 & 0 & -D_1\\ 0 & 1 & 0 & -D_1'\\ D_1' & -D_1 & 1 & 0\\ 0 & 0 & 0 & 1\end{pmatrix}. \tag{15}$$

Here $\mathbf{M_{ir}}$ is the reverse of $\mathbf{M_i}$ ($i=1,2,3,4$). The reverse of an energy chirp ($h$) or momentum compaction ($\xi$) flips

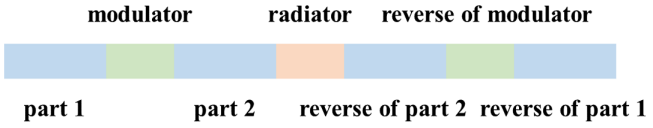


FIG. 7. Schematic layout of a reversible lattice approach. Blue blocks are dispersive lattices. Components following the radiator are the reverse of their counterparts ahead.

the sign. The transfer matrix of the reversible lattice unit is $\mathbf{M_{rev}} = \mathbf{M}_{1r}M_{\mathbf{2r}}\mathbf{M_{3r}}\mathbf{M_{4r}}\mathbf{M_4}\mathbf{M_3}\mathbf{M_2}\mathbf{M_1}$:

$$\mathbf{M_{rev}} = \begin{pmatrix} 1 & 0 & 0 & 0 \\ 0 & 1 & 0 & 0 \\ 0 & 0 & 1 & 0 \\ 0 & 0 & 0 & 1 \end{pmatrix}. \tag{16}$$

It is an I-map, allowing the beam to recover its initial status. In addition to debunching and decoupling, this approach achieves perfect cancellation of the two modulations, not just for linear energy chirp but for modulations of any waveform. The modulations directly add up and cancel each other, as the lattice in between is transparent. This inherent nature of the reversible lattice layout approach could assist with addressing nonlinear issues.

### D. General case

Both the symmetric and reversible lattice layouts have effectively eliminated the influence imposed on the beam in linear beam dynamics, as demonstrated by the map of the unit in Eqs. (13) and (16). It is important to note that modulation cancellation is not always required or essential. A matrix analysis may help to explain:

$$\mathbf{M_{tot}} = \begin{pmatrix} \mathbf{A} & \mathbf{B} \\ \mathbf{C} & \mathbf{E} \end{pmatrix}. \tag{17}$$

Here $\mathbf{A}$, $\mathbf{B}$, $\mathbf{C}$, and $\mathbf{E}$ are $2 \times 2$ submatrices of the transfer map of the whole unit $\mathbf{M_{tot}}$. The decoupling requirement states that $\mathbf{B} = \mathbf{0}$ and $\mathbf{C} = \mathbf{0}$. Regarding $\mathbf{A}$ and $\mathbf{E}$, they are allowed to be functions of the modulation strength $h$. In this case, a more general layout of the lattice can be designed, as depicted in Fig. 8.

Here, the lattice between the modulators is treated as a single entity and its transfer matrix is represented by:

$$\mathbf{M_{mid}} = \begin{pmatrix} 1 & 0 & 0 & a \\ 0 & 1 & 0 & b \\ -b & a & 1 & c \\ 0 & 0 & 0 & 1 \end{pmatrix}. \tag{18}$$

Here $(a, b)$ and $c$ represent the dispersive terms and momentum compaction, respectively. For the lattices at the entrance and exit of the unit, the corresponding transfer matrices are given by:


FIG. 8. Schematic layout of a general lattice approach.

$$\mathbf{M_{ent}} = \begin{pmatrix} 1 & 0 & 0 & f \\ 0 & 1 & 0 & g \\ -g & f & 1 & 0 \\ 0 & 0 & 0 & 1 \end{pmatrix}, \quad \mathbf{M_{ext}} = \begin{pmatrix} 1 & 0 & 0 & p \\ 0 & 1 & 0 & q \\ -q & p & 1 & 0 \\ 0 & 0 & 0 & 1 \end{pmatrix}. \tag{19}$$

Similarly, $(f, g)$ and $(p, q)$ represent the dispersive terms. In these matrices, elements that do not contribute to coupling effects are simplified. Additionally, for the modulators, their transfer matrices are as follows:

$$\mathbf{M_{h1}} = \begin{pmatrix} 1 & 0 & 0 & 0 \\ 0 & 1 & 0 & 0 \\ 0 & 0 & 1 & 0 \\ 0 & 0 & h_1 & 1 \end{pmatrix}, \quad \mathbf{M_{h2}} = \begin{pmatrix} 1 & 0 & 0 & 0 \\ 0 & 1 & 0 & 0 \\ 0 & 0 & 1 & 0 \\ 0 & 0 & h_2 & 1 \end{pmatrix}. \tag{20}$$

Here $h_1$ and $h_2$ represent the modulation strengths of the corresponding modulators.

To achieve the decoupling of the whole unit, whose transfer matrix is $\mathbf{M_{tot}} = \mathbf{M_{ext}}\mathbf{M_{h2}}\mathbf{M_{mid}}\mathbf{M_{h1}}\mathbf{M_{ent}}$, the following four conditions need to be satisfied:

$$-(h_1 + h_2 + ch_1h_2) = \frac{b}{q}h_1 = \frac{a}{p}h_1 = \frac{b}{g}h_2 = \frac{a}{f}h_2. \tag{21}$$

The symmetric and reversible lattice layouts are two specific scenarios within the general approach above. In both cases, the conditions $a = 0$, $b = 0$, and $h_1 + h_2 + ch_1h_2 = 0$ are satisfied. In the symmetric layout, the choice is made to set $h_2 = h_1$ and $ch_1 = -2$. While the reversible layout involves $h_2 = -h_1$ and $c = 0$.

The general lattice layout approach offers a wide range of solutions. This flexibility can be beneficial for designing practical lattices.

## IV. LINEAR BEAM DYNAMICS OF GLSF

This section will focus on studying the linear beam dynamics within the context of the GLSF approach. Specifically, bunch compression, modulation cancellation, and vertical-longitudinal decoupling will be explored.

The case of vertical-longitudinal coupling is examined as an exemplification of transverse-longitudinal coupling schemes. The concept of the reversible lattice layout approach mentioned in Sec. III C is partially employed, where the modulations are canceled.

The GLSF unit is inserted in the radiation section of the ring, as shown in Fig. 9. It can be decomposed into four lattice segments, each separated by two modulators and one radiator. In contrast to the simplified matrices used for algebraic manipulation in the previous section, here the matrices are presented accurately to ensure practical applicability. In addition to Mod1 and Mod2, there is a laser modulator, Mod0, situated outside the GLSF unit within

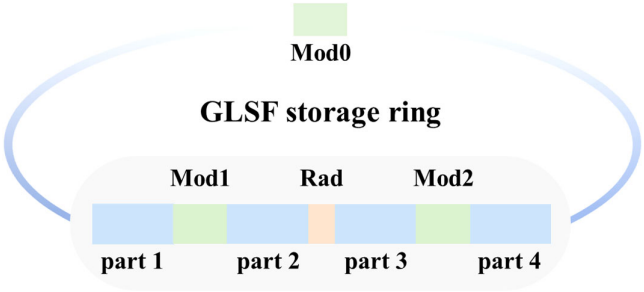


FIG. 9. Diagram showing a storage ring with a GLSF unit. The GLSF unit consists of four lattice segments (parts 1–4), two modulators (Mod1, Mod2), and one radiator (Rad).

the storage ring. The purpose and parameters of Mod0 are discussed in Secs. II C and V B.

### A. Bunch compression

Bunch compression is performed in the first half of the GLSF unit, which consists of part 1, Mod1, and part 2. The corresponding transfer matrices are as follows:

$$\mathbf{M_{part\_2}} = \begin{pmatrix} n_{33} & n_{34} & 0 & n_{36} \\ n_{43} & n_{44} & 0 & n_{46} \\ n_{53} & n_{54} & 1 & n_{56} \\ 0 & 0 & 0 & 1 \end{pmatrix} \quad \mathbf{M_{M1}} = \begin{pmatrix} 1 & 0 & 0 & 0 \\ 0 & 1 & 0 & 0 \\ 0 & 0 & 1 & 0 \\ 0 & 0 & h & 1 \end{pmatrix}$$

$$\mathbf{M_{part\_1}} = \begin{pmatrix} m_{33} & m_{34} & 0 & m_{36} \\ m_{43} & m_{44} & 0 & m_{46} \\ m_{53} & m_{54} & 1 & m_{56} \\ 0 & 0 & 0 & 1 \end{pmatrix}. \tag{22}$$

Here, the letters $m$ and $n$ are used as labels for part 1 and part 2, respectively. The symplectic conditions on the matrix elements [20] are as follows:

$$\begin{aligned} r_{33}r_{44} - r_{34}r_{43} &= 1, \\ r_{36}r_{43} - r_{33}r_{46} &= r_{53}, \\ r_{36}r_{44} - r_{34}r_{46} &= r_{54}. \end{aligned} \tag{23}$$

The transfer matrix from the entrance of the unit to the radiator is given by $\mathbf{M_t} = \mathbf{M_{part\_2}}\mathbf{M_{M1}}\mathbf{M_{part\_1}}$, with the following elements:

$$\begin{aligned} t_{55} &= 1 + hn_{56}, \\ t_{56} &= m_{36}n_{53} + m_{46}n_{54} + n_{56} + m_{56}(1 + hn_{56}). \end{aligned} \tag{24}$$

The bunch compression conditions are therefore:

$$\begin{aligned} 1 + hn_{56} &= 0, \\ m_{36}n_{53} + m_{46}n_{54} + n_{56} &= 0. \end{aligned} \tag{25}$$

These conditions are consistent with Eq. (6) when the momentum compaction $n_{56}$ is substituted for $\xi$ and the dispersive terms ($m_{36}$, $m_{46}$, $n_{53}$, $n_{54}$) are used in place of ($D_1$, $D_1'$, $-D_2'$, $D_2$).

When Eq. (25) is satisfied, the particle position at the radiator $z_{\mathrm{rad}}$ can be expressed as follows:

$$z_{\mathrm{rad}} = t_{53}y_{\mathrm{i}} + t_{54}y_{\mathrm{i}}'. \tag{26}$$

Here, $t_{53}$ and $t_{54}$ are composed of the dispersive terms:

$$\begin{aligned} t_{53} &= m_{33}n_{53} + m_{43}n_{54}, \\ t_{54} &= m_{34}n_{53} + m_{44}n_{54}. \end{aligned} \tag{27}$$

The bunch length at the radiator $\sigma_z(\mathrm{Rad})$ is then:

$$\begin{aligned} \sigma_z(\mathrm{Rad}) &= \sqrt{\epsilon_y \mathcal{H}_y(\mathrm{Rad})}, \\ \mathcal{H}_y(\mathrm{Rad}) &= t_{53}^2\beta_{y\mathrm{i}} - 2t_{53}t_{54}\alpha_{y\mathrm{i}} + t_{54}^2\gamma_{y\mathrm{i}}. \end{aligned} \tag{28}$$

It is worth noting that the bunch length at the radiator is solely determined by the vertical emittance $\epsilon_y$ and a lattice-specific function $\mathcal{H}_y$, which will be explained in detail in Sec. IV B.

The bunching factor, denoted as $b$, quantifies the extent of the bunching of particles. The power of coherent radiation, represented by $P_{\mathrm{rad}}$, is directly proportional to the square of the bunching factor, i.e., $P_{\mathrm{rad}} \propto b^2$.

For a beam with a Gaussian distribution and an rms bunch length of $\sigma_z(\mathrm{Rad})$, the bunching factor $b_0$ at radiation wavelength $\lambda_{\mathrm{r}}$ is given by:

$$b_0 = e^{-\frac{1}{2}k_{\mathrm{r}}^2\sigma_z^2(\mathrm{Rad})}. \tag{29}$$

Here $k_{\mathrm{r}} = \frac{2\pi}{\lambda_{\mathrm{r}}}$ represents the wave number of the radiation. The bunching factor $b_0$ varies between 0 and 1 and decreases as the bunch length $\sigma_z(\mathrm{Rad})$ increases, indicating a deterioration in both the bunching behavior and radiation power.

Note that the bunching factor in Eq. (29) assumes a Gaussian-distributed beam at the radiator. When considering the nonlinear nature of the sinusoidal modulation at Mod1, however, this assumption no longer holds true. The bunch lengthening that occurs at Mod1 causes a degradation of the bunching factor for a prebunched beam. To quantify this reduction in the bunching factor, a reduction factor $R$ is introduced [30]:

$$R = \left| \sum_{p=-\infty}^{\infty} J_p(n) e^{-\frac{1}{2}(n-p)^2 k_{\mathrm{m}}^2 \sigma_z^2(\mathrm{Mod})} \right|. \tag{30}$$

Here, $\sigma_z(\mathrm{Mod})$ represents the bunch length at the modulator Mod1, $k_{\mathrm{m}} = \frac{2\pi}{\lambda_{\mathrm{m}}}$ is the modulation wave number,

$\lambda_m$ is the modulation wavelength, $n = \frac{k_r}{k_m} = \frac{\lambda_m}{\lambda_r}$ is the harmonic number, and $J_p$ is the $p$th order Bessel function of the first kind. The reduction factor $R$ decreases as the bunch length at Mod1 $\sigma_z(\mathrm{Mod})$ increases. The upper and lower limits of $R$ are 1 and $|J_n(n)|$, respectively.

Due to the dispersive placement of Mod1, the bunch length at Mod1 is determined by both the longitudinal and vertical emittances, which is expressed as follows:

$$\sigma_z(\mathrm{Mod}) = \sqrt{\sigma_{z\_z}^2(\mathrm{Mod}) + \sigma_{z\_y}^2(\mathrm{Mod})} = \sqrt{\epsilon_z \beta_{z\mathrm{m}} + \epsilon_y \mathcal{H}_y(\mathrm{Mod})}. \quad (31)$$

Here $\beta_{z\mathrm{m}}$ and $\mathcal{H}_y(\mathrm{Mod})$ represent the longitudinal beta function and $\mathcal{H}$ function at Mod1.

The bunching factor at the radiator in a GLSF SSMB storage ring, denoted as $b$, is then given by the product of $b_0$ and $R$ [30]:

$$b = e^{-\frac{1}{2}k_r^2\sigma_z^2(\mathrm{Rad})} \left| \sum_{p=-\infty}^{\infty} J_p(n) e^{-\frac{1}{2}(n-p)^2 k_m^2 \sigma_z^2(\mathrm{Mod})} \right|. \quad (32)$$

To achieve a large bunching factor, it is necessary to have short bunch lengths at both the radiator and Mod1. However, the reduction of $\sigma_z(\mathrm{Mod})$ and $\sigma_z(\mathrm{Rad})$ is limited since their product must satisfy the inequality [30]:

$$\sigma_{z\_y}(\mathrm{Mod})\sigma_z(\mathrm{Rad}) \geq \frac{\epsilon_y}{|h|}. \quad (33)$$

Here $|h|$ is the modulation strength. Based on Eq. (31), which states $\sigma_{z\_y}(\mathrm{Mod}) = \sqrt{\epsilon_y \mathcal{H}_y(\mathrm{Mod})}$, and given that $\sigma_z(\mathrm{Rad}) = \sqrt{\epsilon_y \mathcal{H}_y(\mathrm{Rad})}$, the lower limit of $\mathcal{H}_y(\mathrm{Mod})$ can be determined as $\frac{1}{h^2 \mathcal{H}_y(\mathrm{Rad})}$.

Through the vertical eigenemittance $\epsilon_y$, a connection is established between the bunch lengths $\sigma_z$ (and therefore the bunching factor $b$ and power of coherent radiation $P_{\mathrm{rad}}$) and the modulation strength $|h|$ (and power of the modulation laser $P_{\mathrm{laser}}$). Alternatively, Eq. (33) can be expressed as $|h| \geq \frac{\epsilon_y}{\sigma_{z\_y}(\mathrm{Mod})\sigma_z(\mathrm{Rad})}$. This implies a reduction in the demand for modulation laser power when considering a given power of coherent radiation by exploiting the nature of low vertical eigenemittance of a planar horizontal-vertical-uncoupled storage ring. This is the exact gist of the GLSF scheme.

For parameter estimation, assuming a modulation laser power of $P_{\mathrm{laser}} = 1$ MW, the modulation strength $|h|$ is approximately 4000 $\mathrm{m}^{-1}$ for a modulation wavelength of $\lambda_m = 1$ μm and a beam energy of $E_s = 400$ MeV. Considering $\epsilon_y = 1$ pmrad, $\lambda_r = 13.5$ nm, and $\sigma_{z\_z}(\mathrm{Mod}) = 50$ nm, the variation of the bunching factor at the radiator $b$, its components $b_0$ and $R$, and the bunch length at Mod1 $\sigma_z(\mathrm{Mod})$ with respect to the bunch length at the radiator $\sigma_z(\mathrm{Rad})$ is illustrated in Fig. 10, while setting $\sigma_{z\_y}(\mathrm{Mod})$ to its minimum defined by Eq. (33) with $\mathcal{H}_y(\mathrm{Mod}) = \frac{1}{h^2 \mathcal{H}_y(\mathrm{Rad})}$.

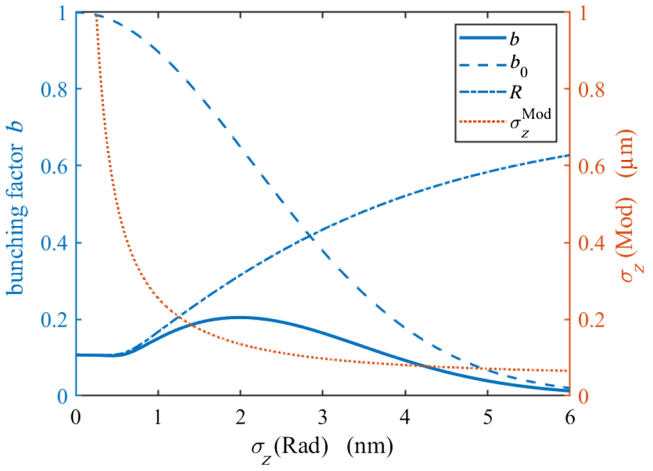


FIG. 10. The variation of the bunching factor at the radiator $b$ (solid), its components $b_0$ (dashed) and $R$ (dash-dotted) (left $y$ axis, blue), and the bunch length at Mod1 $\sigma_z(\mathrm{Mod})$ (dotted, right $y$ axis, orange) as functions of the bunch length at the radiator $\sigma_z(\mathrm{Rad})$, assuming $P_{\mathrm{laser}} = 1$ MW, $|h| = 4000\,\mathrm{m}^{-1}$, $E_s = 400$ MeV, $\epsilon_y = 1$ pmrad, $\lambda_m = 1$ μm, $\lambda_r = 13.5$ nm, $\sigma_{z\_z}(\mathrm{Mod}) = 50$ nm, $\mathcal{H}_y(\mathrm{Mod}) = \frac{1}{h^2 \mathcal{H}_y(\mathrm{Rad})}$.

It is observed in Fig. 10 that the bunching factor $b$ remains relatively constant until $\sigma_z(\mathrm{Rad})$ reaches 0.6 nm. Beyond this point, the bunching factor increases, peaking at 2 nm of $\sigma_z(\mathrm{Rad})$, and then declines as $\sigma_z(\mathrm{Rad})$ continues to rise. Both $b_0$ and $R$ exhibit negligible changes and approach their limits when $\sigma_z(\mathrm{Rad})$ is reduced to 0 and $\sigma_z(\mathrm{Mod})$ becomes significant. It explains the plateau in $b$ before reaching $\sigma_z(\mathrm{Rad}) = 0.6$ nm. Once it is surpassed, noticeable changes occur in $b_0$ and $R$, with increasing $\sigma_z(\mathrm{Rad})$ resulting in a decrease in $\sigma_z(\mathrm{Mod})$, $b_0$, and an increase in $R$. Consequently, the overall bunching factor initially increases and subsequently decreases.

In this illustrative case, a bunching factor greater than 0.1 can be achieved with a low modulation laser power of 1 MW. This indicates the significant potential for generating kW-level quasicontinuous-wave 13.5-nm EUV radiation in a GLSF SSMB storage ring, as demonstrated later in this paper.

### B. $\mathcal{H}$ function

The $\mathcal{H}$ function holds great importance in the GLSF approach, particularly in obtaining a short bunch length at the radiator. This subsection begins by examining the two expressions of the $\mathcal{H}$ function, followed by an investigation into its evolution rule and exploration of methods to achieve a small value for it.

Consider a general lattice with vertical dispersion and no laser modulators positioned within it. The transfer matrix in the $(y, y', z, \delta)$ dimensions can be represented as follows, where the elements $(r_{35}, r_{45}, r_{63}, r_{64}, r_{65})$ are eliminated due to the absence of the coupling induced by energy modulation:

$$\mathbf{M_{general\_lattice}} = \begin{pmatrix} r_{33} & r_{34} & 0 & r_{36} \\ r_{43} & r_{44} & 0 & r_{46} \\ r_{53} & r_{54} & 1 & r_{56} \\ 0 & 0 & 0 & 1 \end{pmatrix}. \tag{34}$$

Subscripts are used to represent parameters at the entrance of the lattice (denoted as $i$) and at the exit (denoted as $f$). The deduction of the bunch length at the exit, denoted as $\sigma_{zf}$, involves the following equations:

$$\begin{aligned} z_{\mathrm{f}} &= r_{53} y_{\mathrm{i}} + r_{54} y'_{\mathrm{i}} + z_{\mathrm{i}} + r_{56}\delta_{\mathrm{i}}, \\ \sigma_{z\mathrm{f}}^2 &= \epsilon_y \mathcal{H}_{y\_1} + \epsilon_z \beta_{z\mathrm{f}}, \\ \mathcal{H}_{y\_1} &= r_{53}^2 \beta_{y\mathrm{i}} - 2 r_{53} r_{54} \alpha_{y\mathrm{i}} + r_{54}^2 \gamma_{y\mathrm{i}}. \end{aligned} \tag{35}$$

Here, $\mathcal{H}_{y\_1}$ represents the first kind of expression of the $\mathcal{H}$ function, which is consistent with the form presented in Eq. (28). It quantifies the bunch lengthening resulting from the vertical emittance.

Starting from $\mathcal{H}_{y\_1}$, an alternative expression of the $\mathcal{H}$ function, denoted as $\mathcal{H}_{y\_2}$, can be derived by replacing $(r_{53}, r_{54}, \alpha_{y\mathrm{i}}, \beta_{y\mathrm{i}}, \gamma_{y\mathrm{i}})$ with $(r_{36}, r_{46}, \alpha_{y\mathrm{f}}, \beta_{y\mathrm{f}}, \gamma_{y\mathrm{f}})$. The substitution law is given by:

$$\begin{aligned} &(r_{53}, r_{54}, \alpha_{y\mathrm{i}}, \beta_{y\mathrm{i}}, \gamma_{y\mathrm{i}})^{\intercal} = \mathbf{X}(r_{36}, r_{46}, \alpha_{y\mathrm{f}}, \beta_{y\mathrm{f}}, \gamma_{y\mathrm{f}})^{\intercal}, \\ &\mathbf{X} = \begin{pmatrix} r_{43} & -r_{33} & 0 & 0 & 0 \\ r_{44} & -r_{34} & 0 & 0 & 0 \\ 0 & 0 & r_{33}r_{44} + r_{34}r_{43} & r_{43}r_{44} & r_{33}r_{34} \\ 0 & 0 & 2r_{34}r_{44} & r_{44}^2 & r_{34}^2 \\ 0 & 0 & 2r_{33}r_{43} & r_{43}^2 & r_{33}^2 \end{pmatrix}. \end{aligned} \tag{36}$$

The symplectic condition $r_{33}r_{44} - r_{34}r_{43} = 1$ is used in simplification. Then there is:

$$\mathcal{H}_{y\_2} = r_{46}^2 \beta_{y\mathrm{f}} + 2 r_{36} r_{46} \alpha_{y\mathrm{f}} + r_{36}^2 \gamma_{y\mathrm{f}}. \tag{37}$$

Furthermore, assuming dispersion-free conditions at the entrance of the lattice, the parameters $(r_{36}, r_{46})$ can be redefined as the dispersion functions at the lattice exit, denoted as $(D_{\mathrm{f}}, D'_{\mathrm{f}})$. Consequently, the second form of the $\mathcal{H}$ function can also be expressed as $\mathcal{H}_{y\_2} = D'^2_{\mathrm{f}} \beta_{y\mathrm{f}} + 2 D_{\mathrm{f}} D'_{\mathrm{f}} \alpha_{y\mathrm{f}} + D_{\mathrm{f}}^2 \gamma_{y\mathrm{f}}$. Moreover, at any given position $s$ within the lattice, the corresponding $\mathcal{H}$ function can be represented as:

$$\mathcal{H}_{y\_2}(s) = \left(D'^2 \beta_y + 2 D D' \alpha_y + D^2 \gamma_y\right)_s. \tag{38}$$

The introduction of multiple forms of the $\mathcal{H}$ function serves the purpose of facilitating a deeper understanding and offering flexibility in the selection of the most appropriate and convenient expression for a given situation. In general, $\mathcal{H}_{y\_1}$ is inherently intuitive and applicable across a wide range of circumstances, including cases involving laser modulators as demonstrated in previous sections. On the other hand, $\mathcal{H}_{y\_2}$ proves valuable for comprehending the evolution of the $\mathcal{H}$ function from the perspective of normalized dispersion coordinates, as illustrated later in this subsection.

While $\mathcal{H}_{y\_1}$ quantifies the extent of bunch lengthening caused by the vertical emittance, $\mathcal{H}_{y\_2}(s)$ is commonly referred to in the community as a coefficient specifying the excitation of vertical betatron oscillation amplitude resulting from energy changes during photon emission [37]. Both expressions capture the coupling effects between dimensions, with one acting from $(y, y')$ to $z$ and the other from $\delta$ to $(y, y')$. These cross-plane couplings are intricately intertwined by symplecticity-imposed constraints [20]. In essence, they represent two sides of the same coin in beam dynamics.

The deduction above of $\mathcal{H}_{y\_2} = \mathcal{H}_{y\_1}$ assumes the absence of laser modulators in the lattice. However, with the introduction of laser modulators, the relationship between $(r_{53}, r_{54})$ and $(r_{36}, r_{46})$ becomes more complex due to the symplectic condition requirements. Consequently, the general validity of $\mathcal{H}_{y\_2} = \mathcal{H}_{y\_1}$ is compromised.

Fortunately, in the context of the GLSF unit, the expression $\mathcal{H}_{y\_2}$ remains applicable for quantifying bunch lengthening at the radiator. This is because the bunch compression condition $1 + h n_{56} = 0$ effectively eliminates the influence of part 1 on both bunch lengthening and $\mathcal{H}_y$. Considering a hypothetical component that is placed immediately after the laser modulator Mod1 and provides a lumped momentum compaction of $n_{56}$, the corresponding transfer matrix is:

$$\mathbf{M_{n56}} = \begin{pmatrix} 1 & 0 & 0 & 0 \\ 0 & 1 & 0 & 0 \\ 0 & 0 & 1 & n_{56} \\ 0 & 0 & 0 & 1 \end{pmatrix}. \tag{39}$$

The transfer matrix of the lattice, comprising in sequence part 1, Mod1, and the hypothetical component, can be expressed as $\mathbf{M_r} = \mathbf{M_{n56}} \mathbf{M_{M1}} \mathbf{M_{part\_1}}$ with elements:

$$\begin{aligned} r_{53} &= m_{53}(1 + h n_{56}) = 0, \\ r_{54} &= m_{54}(1 + h n_{56}) = 0. \end{aligned} \tag{40}$$

As mentioned earlier, there is no contribution to bunch lengthening and $\mathcal{H}_y$ from $(m_{53}, m_{54})$ of part 1. In other words, the bunch length at the radiator $\sigma_z$ (Rad) is solely determined by part 2:

$$\begin{aligned}\mathcal{H}_y(\mathrm{Rad}) &= n_{53}^2\beta_{\mathrm{ym}} - 2n_{53}n_{54}\alpha_{\mathrm{ym}} + n_{54}^2\gamma_{\mathrm{ym}} \\ &= n_{46}^2\beta_{\mathrm{yr}} + 2n_{36}n_{46}\alpha_{\mathrm{yr}} + n_{36}^2\gamma_{\mathrm{yr}}. \end{aligned} \tag{41}$$

Here, $(\alpha_{\mathrm{ym}}, \beta_{\mathrm{ym}}, \gamma_{\mathrm{ym}})$ and $(\alpha_{\mathrm{yr}}, \beta_{\mathrm{yr}}, \gamma_{\mathrm{yr}})$ are, respectively, the Courant-Snyder functions evaluated at Mod1 and the radiator. Notably, since part 2 does not involve any laser modulators, the validity of $\mathcal{H}_{y\_2}$ is restored within this specific context.

According to Eq. (28), achieving a short bunch length of 3 nm at the radiator requires a value as low as 9 μm for the $\mathcal{H}_y$ function, assuming an $\epsilon_y$ of 1 pm rad. To accomplish this, the evolution of $\mathcal{H}_y$ is investigated in magnets, including dipoles and quadrupole channels (alternately arranged quadrupoles and drifts). As mentioned earlier, the expression $\mathcal{H}_{y\_2}$ is employed in the analysis.

It is worth noting that there is a resemblance between the expression $\mathcal{H}_{y\_2}(s)$ and the Courant-Snyder invariant $\epsilon_u$ $(u = x, y)$:

$$\begin{aligned}\mathcal{H}_y(s) &= (D'^2\beta_y + 2DD'\alpha_y + D^2\gamma_y)_s, \\ \epsilon_u &= u'^2\beta_u + 2uu'\alpha_u + u^2\gamma_u. \end{aligned} \tag{42}$$

This resemblance suggests that the application of normal or canonical form could also be employed here to clarify the beam dynamics in the evolution of the $\mathcal{H}$ function. The $\mathcal{H}_y$ function can be expressed as follows:

$$\begin{aligned}\mathcal{H}_y(s) &= (v^2 + p_v^2)_s, \\ (v, p_v) &= \left(\frac{D}{\sqrt{\beta_y}}, \frac{\alpha_y D + \beta_y D'}{\sqrt{\beta_y}}\right). \end{aligned} \tag{43}$$

A transformation from the physical coordinates $(D, D')$ to the normalized coordinates $(v, p_v)$ is performed:

$$\begin{pmatrix} v \\ p_v \end{pmatrix} = \mathbf{A}\begin{pmatrix} D \\ D' \end{pmatrix}, \qquad \mathbf{A}(s) = \begin{pmatrix} \frac{1}{\sqrt{\beta_y(s)}} & 0 \\ \frac{\alpha_y(s)}{\sqrt{\beta_y(s)}} & \sqrt{\beta_y(s)} \end{pmatrix}. \tag{44}$$

Here, the matrix $\mathbf{A}(s)$ denotes a static coordinate transformation. Thus, the $\mathcal{H}_y$ function represents the square of the Euclidean norm of the vector $(v, p_v)$ in the normalized phase space. The evolution of $(v, p_v)$ is therefore crucial for measuring $\mathcal{H}_y$.

To account for the complete beam dynamics, the matrix $\mathbf{R}$ is introduced:

$$\mathbf{R} = \begin{pmatrix} \cos\psi & \sin\psi \\ -\sin\psi & \cos\psi \end{pmatrix}. \tag{45}$$

This matrix $\mathbf{R}$ denotes the clockwise rotation of the vector $(v, p_v)$ in the normalized phase space, where the rotation angle $\psi$ corresponds to the betatron phase advance. Then a transfer map in $(y, y')$ dimensions, spanning from the initial point $s_1$ to the final point $s_2$, can be decomposed as follows:

$$\mathbf{M}(s_2|s_1) = \mathbf{A^{-1}}(s_2)\mathbf{R}\mathbf{A}(s_1). \tag{46}$$

In other words, the effect of $\mathbf{M}(s_2|s_1)$ can be interpreted as three sequential steps: first, a transformation from the physical coordinates $(D, D')$ to the normalized coordinates $(v, p_v)$ by $\mathbf{A}(s_1)$ at position $s_1$; then, a rotation in the normalized coordinate space by $\mathbf{R}$; and finally, a transformation from the normalized coordinates $(v, p_v)$ back to the physical coordinates $(D, D')$ by $\mathbf{A^{-1}}(s_2)$ at position $s_2$. It is important to note that the transformation $\mathbf{A}$ is static, while the dynamics are encapsulated within the parameter $\psi$ of the rotation matrix $\mathbf{R}$.

The evolution of the vector $(v, p_v)$ in magnets is investigated, considering the following cases: (a) a quadrupole channel, (b) a dipole, and (c) a unit with two dipoles and one quadrupole channel. The relationship between the vectors at the beginning point $s_1$ and the end point $s_2$ is depicted in Fig. 11 and Eqs. (47), (48), and (51).

$$\begin{aligned}\begin{pmatrix} v \\ p_v \end{pmatrix}_2 &= \mathbf{A}(s_2)\begin{pmatrix} D \\ D' \end{pmatrix}_2 \\ &= \mathbf{A}(s_2)\mathbf{M}(s_2|s_1)\begin{pmatrix} D \\ D' \end{pmatrix}_1 \\ &= \mathbf{R}\mathbf{A}(s_1)\begin{pmatrix} D \\ D' \end{pmatrix}_1 = \mathbf{R}\begin{pmatrix} v \\ p_v \end{pmatrix}_1. \end{aligned} \tag{47}$$

$$\begin{aligned}\begin{pmatrix} v \\ p_v \end{pmatrix}_2 &= \mathbf{A}(s_2)\begin{pmatrix} D \\ D' \end{pmatrix}_2 \\ &= \mathbf{A}(s_2)\left(\mathbf{M}(s_2|s_1)\begin{pmatrix} D \\ D' \end{pmatrix}_1 + \begin{pmatrix} \rho(1-\cos\theta) \\ \sin\theta \end{pmatrix}\right) \\ &= \mathbf{R}\begin{pmatrix} v \\ p_v \end{pmatrix}_1 + \mathbf{Dv}. \end{aligned} \tag{48}$$

The investigation begins with the case of a quadrupole channel. As shown in Fig. 11(a) and Eq. (47), the evolution of the normalized vector $(v, p_v)$ involves rotation solely. This observation suggests that the $\mathcal{H}_y$ function remains invariant throughout quadrupole channels, as no additional dispersion is imposed.

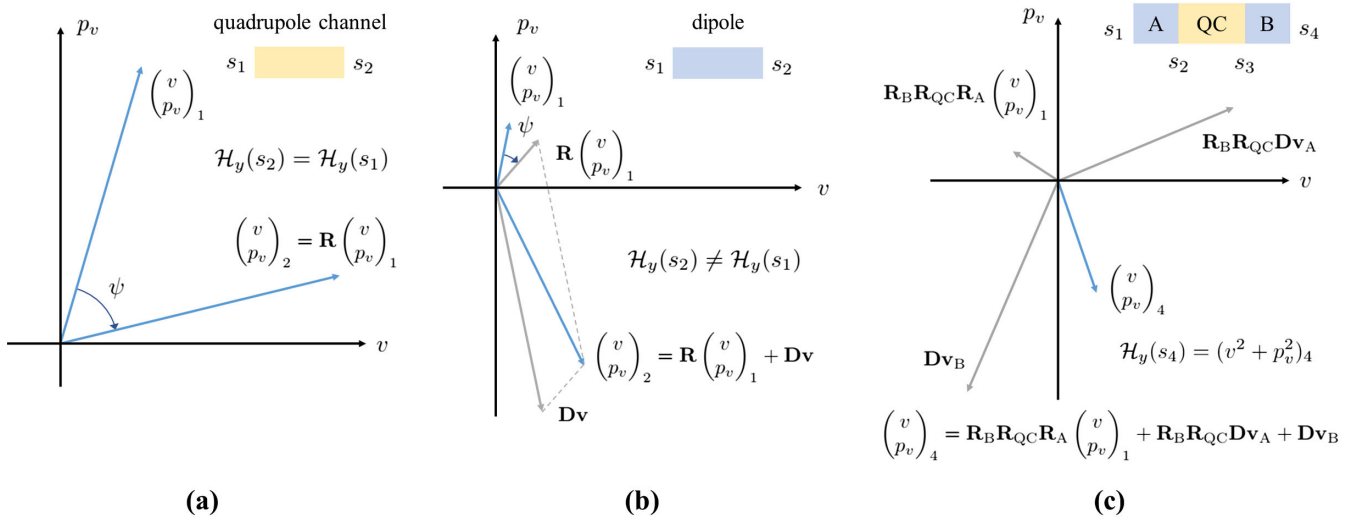


FIG. 11. Sketch showing the evolution of $(v, p_v)$ in the normalized phase space in (a) a quadrupole channel, (b) a dipole, and (c) a unit with two dipoles and one quadrupole channel.

The case of dipoles, however, is different compared to quadrupole channels. Dispersion-induced driving terms **Dv**, as shown in Eq. (48), are generated:

$$\mathbf{Dv} = \begin{pmatrix} \frac{1}{\sqrt{\beta_y}}\rho(1-\cos\theta) \\ \frac{\alpha_y}{\sqrt{\beta_y}}\rho(1-\cos\theta) + \sqrt{\beta_y}\sin\theta \end{pmatrix}. \tag{49}$$

Here, $(\rho, \theta)$ represent the bending radius and angle of a dipole, while $(\alpha_y, \beta_y)$ are the Courant-Snyder functions at the exit. Based on Fig. 11(b) and Eq. (48), it is evident that the vector $(v, p_v)$ at the end of a dipole is obtained by combining the rotating term originating from the initial $(v, p_v)$ and the driving term **Dv**. In general, $\mathcal{H}_y$ changes over a dipole.

It should be noted that the analysis above specifically addresses sector dipoles with no longitudinal gradient. The edge effect of rectangular dipoles can be handled in nearby quadrupole channels, while dipoles with gradients can be divided into slices with constant field strengths.

Once the evolution rule of the $\mathcal{H}$ function has been established for both quadrupole channels and dipoles, it becomes possible to explore more complex scenarios. In this regard, a case involving two dipoles and a quadrupole channel is investigated, as illustrated in Fig. 11(c). By applying the rules outlined in Eqs. (47) and (48), the evolution of the vector $(v, p_v)$ can be described as follows:

$$\begin{aligned} \begin{pmatrix} v \\ p_v \end{pmatrix}_4 &= \mathbf{R}_\mathrm{B}\begin{pmatrix} v \\ p_v \end{pmatrix}_3 + \mathbf{Dv}_\mathrm{B}; \\ \begin{pmatrix} v \\ p_v \end{pmatrix}_3 &= \mathbf{R}_\mathrm{QC}\begin{pmatrix} v \\ p_v \end{pmatrix}_2; \\ \begin{pmatrix} v \\ p_v \end{pmatrix}_2 &= \mathbf{R}_\mathrm{A}\begin{pmatrix} v \\ p_v \end{pmatrix}_1 + \mathbf{Dv}_\mathrm{A}. \end{aligned} \tag{50}$$

In this context, the subscripts (A, B, QC) refer to the first dipole, the second dipole, and the quadrupole channel in between, respectively. Then there is:

$$\begin{pmatrix} v \\ p_v \end{pmatrix}_4 = \mathbf{R}_\mathrm{B}\mathbf{R}_\mathrm{QC}\mathbf{R}_\mathrm{A}\begin{pmatrix} v \\ p_v \end{pmatrix}_1 + \mathbf{R}_\mathrm{B}\mathbf{R}_\mathrm{QC}\mathbf{Dv}_\mathrm{A} + \mathbf{Dv}_\mathrm{B}. \tag{51}$$

The $\mathcal{H}$ function at the end of this unit is then determined by the initial vector $(v, p_v)$, the driving terms **Dv** of both dipoles, and the rotation angles of the rotation matrices **R** for all three components.

As mentioned earlier, a value of 9 μm is required for the $\mathcal{H}$ function at the radiator $\mathcal{H}_y(\mathrm{Rad})$. The simplest solution involves incorporating a single dipole in part 2 of the GLSF unit, as shown in Fig. 11(b) and Eq. (48). Since quadrupole channels do not contribute, $\mathcal{H}_y(\mathrm{Rad})$ depends solely on the driving term **Dv** of this dipole. To simplify the analysis, the thin-lens approximation is applied, leading to the reduction of Eq. (49) to:

$$\mathbf{Dv} = \begin{pmatrix} 0 \\ \sqrt{\beta_y}\theta \end{pmatrix}. \tag{52}$$

Consequently, there is $\mathcal{H}_y = \|\mathbf{Dv}\|^2 = \beta_y\theta^2$. In this scenario, attaining a $\mathcal{H}_y$ value of 9 μm can present practical challenges due to the demand of a short dipole length.

Alternatively, part 2 can employ a lattice layout with two dipoles and one quadrupole channel, as described in Fig. 11(c) and Eq. (51), for a potential solution. As there is no generation of $\mathcal{H}_y$ prior to this unit, the final vector $(v, p_v)$ in Eq. (51) simplifies to:

$$\begin{pmatrix} v \\ p_v \end{pmatrix} = \mathbf{R}_\mathrm{B}\mathbf{R}_\mathrm{QC}\mathbf{Dv}_\mathrm{A} + \mathbf{Dv}_\mathrm{B}. \tag{53}$$

The idea is to achieve cancellation between the two vectors, $\mathbf{R}_B\mathbf{R}_{QC}\mathbf{Dv}_A$ and $\mathbf{Dv}_B$, to ensure that their residual contribution to $\mathcal{H}_y$ is sufficiently low. The cancellation is true when the following conditions are met:

$$\begin{aligned} \|\mathbf{Dv}_A\| &= \|\mathbf{Dv}_B\|, \\ \phi_{Dv_A} - \psi_{QC} - \psi_B &= \phi_{Dv_B} + \pi + 2k\pi. \\ (k &= 0, \pm 1, \pm 2, \cdots) \end{aligned} \tag{54}$$

Here, $(\phi, \psi)$ represent the phase angle of the vector $(v, p_v)$ in normalized coordinates and the rotation angle of the rotation matrix $R$, respectively. While the rotation angle $\psi$ is clockwise, the phase angle $\phi = \arctan\frac{p_v}{v}$ is defined in a counterclockwise manner. It is worth noting that Eq. (54) serves as a general guideline for minimizing the value of the $\mathcal{H}$ function in a lattice containing two dipoles, such as a double-bend achromat (DBA) unit.

For instance, consider two dipoles with identical bending angles but opposite bending directions. By applying the thin-lens approximation to these dipoles, it can be observed that $\|\mathbf{Dv}_A\| = \sqrt{\beta_{yA}}|\theta|$, $\|\mathbf{Dv}_B\| = \sqrt{\beta_{yB}}|\theta|$, $|\phi_{Dv_A} - \phi_{Dv_B}| = \pi$, and $\psi_B = 0$. Therefore, conditions in Eq. (54) can now be expressed as:

$$\begin{aligned} \beta_{yA} &= \beta_{yB}, \\ \psi_{QC} &= 2k\pi. \\ (k &= 0, \pm 1, \pm 2, \cdots) \end{aligned} \tag{55}$$

Although Eq. (55) is derived based on the thin-lens approximation of the dipoles, these conditions are still approximately satisfied in some practical cases when attempting to minimize the $\mathcal{H}_y$ function.

### C. Modulation cancellation

While the modulation introduced by Mod1 facilitates bunch compression, it is advantageous to cancel out its effects by employing Mod2. This cancellation enables the demodulation and debunching of the beam while eliminating the nonlinearities caused by the sinusoidal modulation. The lattice between the two modulators, involving part 2 and part 3, is specifically designed to achieve modulation cancellation.

Derived from the reversible lattice layout, the modulation of Mod2 should be the reverse of Mod1's. The manipulation functions of Mod1 and Mod2 can be denoted as $f_1$ and $f_2$, satisfying the equation $f_1(z) + f_2(z) = 0$. Specifically, for the linear chirp of Mod1 in Eq. (22), $f_1(z) = hz$. Then $f_2(z) = -hz$, and the corresponding transfer matrix of Mod2 is given as:

$$\mathbf{M_{M2}} = \begin{pmatrix} 1 & 0 & 0 & 0 \\ 0 & 1 & 0 & 0 \\ 0 & 0 & 1 & 0 \\ 0 & 0 & -h & 1 \end{pmatrix}. \tag{56}$$

For a perfect cancellation, the longitudinal positions of particles at Mod1 and Mod2 must be identical, denoted as $z_{M1} = z_{M2}$. This indicates that the lattice between Mod1 and Mod2 should be transparent to particles in the $z$ dimension. The corresponding transfer matrix $\mathbf{M_w} = \mathbf{M_{part\_3}}\mathbf{M_{part\_2}}$ should take the following form:

$$\mathbf{M_w} = \begin{pmatrix} w_{33} & w_{34} & 0 & 0 \\ w_{43} & w_{44} & 0 & 0 \\ 0 & 0 & 1 & 0 \\ 0 & 0 & 0 & 1 \end{pmatrix}. \tag{57}$$

To ensure $z_{M1} = z_{M2}$, the constraints $w_{53} = w_{54} = w_{56} = 0$ and $w_{55} = 1$ are imposed. Additionally, applying the symplectic condition of Eq. (23) yields $w_{36} = w_{46} = 0$.

From Eq. (57), it is evident that the lattice between the two modulators is both achromatic and isochronous. It is important to note that $\mathbf{M_w}$ is not necessarily an I-map. In this case, transportation in the $(y, y')$ phase space is unrestricted, as it does not affect the modulation cancellation. The strict constraint of paired reverse components is relaxed to simplify lattice design. Nevertheless, modulation cancellation through transparency in $z$ is maintained.

$\mathbf{M_{part\_2}}$ has already been given by Eq. (22). The transfer matrices of part 3 and its mirror can be defined as:

$$\begin{aligned} \mathbf{M_{part\_3}} &= \begin{pmatrix} e_{44} & e_{34} & 0 & -e_{54} \\ e_{43} & e_{33} & 0 & -e_{53} \\ -e_{46} & -e_{36} & 1 & e_{56} \\ 0 & 0 & 0 & 1 \end{pmatrix}, \\ \mathbf{M_{part\_3\_mir}} &= \begin{pmatrix} e_{33} & e_{34} & 0 & e_{36} \\ e_{43} & e_{44} & 0 & e_{46} \\ e_{53} & e_{54} & 1 & e_{56} \\ 0 & 0 & 0 & 1 \end{pmatrix}. \end{aligned} \tag{58}$$

Here, part 3 is denoted by the letter $e$, and the symplectic condition in Eq. (23) is satisfied. The motivation behind presenting $\mathbf{M_{part\_3}}$ as shown in Eq. (58) and introducing $\mathbf{M_{part\_3\_mir}}$ is to simplify the algebraic derivation of $\mathbf{M_w}$.

Focusing on the elements of interest, there are:

$$\begin{aligned} w_{53} &= (n_{36} - e_{36})n_{43} - (n_{46} + e_{46})n_{33}, \\ w_{54} &= (n_{36} - e_{36})n_{44} - (n_{46} + e_{46})n_{34}, \\ w_{55} &= 1, \\ w_{56} &= (n_{56} + e_{56}) - (n_{46}e_{36} + n_{36}e_{46}). \end{aligned} \tag{59}$$

The definition of $\mathbf{M}_{\mathbf{part\_3}}$ in Eq. (58) allows the pairing of $(e_{36}, e_{46})$ with $(n_{36}, n_{46})$ in $w_{53}$ and $w_{54}$. Due to the requirement of symplecticity $(n_{33}n_{44} - n_{34}n_{43} = 1)$, it is impossible to have $n_{33} = n_{34} = 0$ or $n_{43} = n_{44} = 0$. To achieve $w_{53} = w_{54} = 0$, the following must be met:

$$\begin{aligned} n_{36} - e_{36} &= 0, \\ n_{46} + e_{46} &= 0. \end{aligned} \tag{60}$$

With Eq. (60), there is $n_{46}e_{36} + n_{36}e_{46} = 0$. Then $w_{56} = 0$ can be rewritten as:

$$n_{56} + e_{56} = 0. \tag{61}$$

Therefore, Eqs. (60) and (61) represent the conditions for modulation cancellation or achieving an achromatic and isochronous lattice between modulators. The conditions in Eq. (60) can also be explained through the continuity of dispersion functions at the radiator, assuming it is dispersion-free at the far ends of part 2 and part 3.

Analyses above are based on two assumptions: (i) The lattice between Mod1 and Mod2 is assumed to be perfectly linear; (ii) the manipulation functions $(f_1, f_2)$ of modulators perfectly cancel each other, i.e., $f_1(z) + f_2(z) = 0$.

However, in reality, these assumptions may not hold true because of the presence of nonlinearity in the lattice and distortion of $(f_1, f_2)$ caused by the intrinsic momentum compaction of undulators. Consequently, achieving perfect cancellation of modulation can be challenging even when the conditions in Eqs. (60) and (61) are satisfied. At the end of the paper, the nonlinear dynamics involved are briefly discussed.

### D. Vertical-longitudinal decoupling

To maintain a low vertical emittance in the ring, which is necessary for bunch compression, it is essential to eliminate the introduced vertical-longitudinal coupling within the GLSF unit. This decoupling is specifically achieved in the final part, part 4.

The remaining coupling terms are examined first. The transfer matrix of the components preceding part 4, denoted as $\mathbf{M}_{\mathbf{v}}$, is given by:

$$\begin{aligned} \mathbf{M}_{\mathbf{v}} &= \mathbf{M}_{\mathbf{M2}}\mathbf{M}_{\mathbf{w}}\mathbf{M}_{\mathbf{M1}}\mathbf{M}_{\mathbf{part\_1}} \\ &= \begin{pmatrix} v_{33} & v_{34} & 0 & v_{36} \\ v_{43} & v_{44} & 0 & v_{46} \\ v_{53} & v_{54} & 1 & v_{56} \\ 0 & 0 & 0 & 1 \end{pmatrix}, \end{aligned} \tag{62}$$

with:

$$\begin{pmatrix} v_{36} \\ v_{46} \end{pmatrix} = \begin{pmatrix} e_{44} & e_{34} \\ e_{43} & e_{33} \end{pmatrix} \begin{pmatrix} n_{33} & n_{34} \\ n_{43} & n_{44} \end{pmatrix} \begin{pmatrix} m_{36} \\ m_{46} \end{pmatrix}. \tag{63}$$

Since the remaining coupling terms are related to dispersion, the objective of part 4 is to ensure an achromatic GLSF unit. The transfer matrices of part 4 and its mirror counterpart are given by:

$$\begin{aligned} \mathbf{M}_{\mathbf{part\_4}} &= \begin{pmatrix} i_{44} & i_{34} & 0 & -i_{54} \\ i_{43} & i_{33} & 0 & -i_{53} \\ -i_{46} & -i_{36} & 1 & i_{56} \\ 0 & 0 & 0 & 1 \end{pmatrix}, \\ \mathbf{M}_{\mathbf{part\_4\_mir}} &= \begin{pmatrix} i_{33} & i_{34} & 0 & i_{36} \\ i_{43} & i_{44} & 0 & i_{46} \\ i_{53} & i_{54} & 1 & i_{56} \\ 0 & 0 & 0 & 1 \end{pmatrix}. \end{aligned} \tag{64}$$

Here, part 4 is denoted by the letter $i$. The symplectic condition in Eq. (23) is satisfied. By employing the approach used in Eqs. (59) and (60), the conditions to achieve an achromat are:

$$\begin{aligned} v_{36} - i_{36} &= 0, \\ v_{46} + i_{46} &= 0. \end{aligned} \tag{65}$$

With Eq. (65) fulfilled, the GLSF unit achieves vertical-longitudinal decoupling.

Flip the direction in which the beam travels. The route (part 1 → Mod1 → part 2 → Rad → part 3 → Mod2 → part 4) now becomes (part 4 flip → Mod2 → part 3 flip → Rad → part 2 flip → Mod1 → part 1 flip), as shown in Fig. 12. Here, "part $X$ flip" represents the mirror of part $X$ (where $X = 1, 2, 3, 4$). The mirrors of Mod1 or Mod2 remain unchanged.

It can be proven that the conditions of bunch compression, modulation cancellation, and vertical-longitudinal decoupling remain valid in the flipped lattice. In other words, the GLSF unit can be inserted in either direction into the SSMB storage ring. This duality arises from the achromatic nature of the GLSF unit.

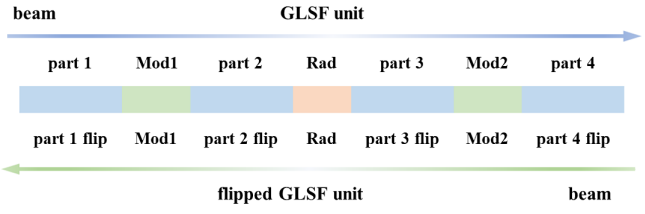


FIG. 12. Sketch illustrating the two ways in which the beam passes through the GLSF unit. Here, part $X$ flip represents the mirror of part $X$ (where $X = 1, 2, 3, 4$).

### E. Linear conditions of the GLSF unit lattice

Listed below is a summary of the linear conditions in the lattice design of a GLSF unit given by Fig. 9:

(i) Bunch compression:

$$1 + hn_{56} = 0,$$
$$m_{36}n_{53} + m_{46}n_{54} + n_{56} = 0,$$
$$\mathcal{H}_y(\mathrm{Rad}) = \frac{\sigma_z^2(\mathrm{Rad})}{\epsilon_y},$$
$$\mathcal{H}_y(\mathrm{Mod}) = \frac{1}{h^2\mathcal{H}_y(\mathrm{Rad})}.$$

(ii) Modulation cancellation:

$$e_{36} - n_{36} = 0,$$
$$e_{46} + n_{46} = 0,$$
$$e_{56} + n_{56} = 0.$$

(iii) Vertical-longitudinal decoupling:

$$i_{36} - v_{36} = 0,$$
$$i_{46} + v_{46} = 0.$$

These conditions can be categorized for each part of the unit:

(i) Part 1

$$m_{36}n_{53} + m_{46}n_{54} + n_{56} = 0,$$
$$\mathcal{H}_y(\mathrm{Mod}) = \frac{1}{h^2\mathcal{H}_y(\mathrm{Rad})}.$$

(ii) Part 2

$$1 + hn_{56} = 0,$$
$$\mathcal{H}_y(\mathrm{Rad}) = \frac{\sigma_z^2(\mathrm{Rad})}{\epsilon_y}.$$

(iii) Part 3

$$e_{36} - n_{36} = 0,$$
$$e_{46} + n_{46} = 0,$$
$$e_{56} + n_{56} = 0.$$

(iv) part 4

$$i_{36} - v_{36} = 0,$$
$$i_{46} + v_{46} = 0.$$

In practical lattice design, achieving precise equality as stated in these conditions can be challenging. It is necessary to analyze the impact of deviations from equality on beam dynamics, including the bunching factor and residual modulation. The tolerance for deviations can thus be estimated.

## V. LINEAR LATTICE REALIZATION

With beam dynamics clarified and the required conditions established, a linear lattice can be realized in practice as a GLSF unit. This section aims to offer details regarding the strategies and settings involved in lattice realization, as well as the parameters and performance of one specific instance of a practical linear lattice.

### A. Strategies and settings

In each part of the unit, a pair of dipoles is positioned between three quadrupole channels, resembling a dogleg configuration. The dipoles bend in opposite directions with identical bending radii and angles, resulting in the beam traveling parallel to its initial direction after passing through. The quadrupole channels offer flexibility for optimization. This configuration enables the generation of the required lattices in a simple and flexible manner.

The GLSF unit is then partitioned into modules comprising quadrupole channels, dipoles, and modulators, as illustrated in Fig. 13. This layout is afterward employed for the realization of the practical lattice.

The realization of the lattice is performed step by step, as handling all the variables and goals of the overall lattice in a single run is impractical. The sequence of part 2, part 3,

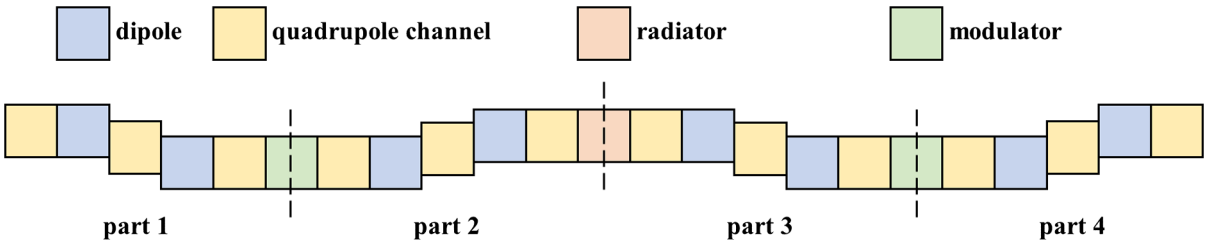


FIG. 13. Sketch showing the modules that compose the GLSF unit. The blocks indicate modules of various kinds, including quadrupole channels (yellow), dipoles (blue), modulators (green), and the radiator (orange).

part 1, and part 4 is followed, considering the necessary conditions and prerequisites of each part.

For the quadrupole channels, a pattern of (quad-quad-⋯-quad-quad) is initially tested before converting it into an equivalent (drift-quad-⋯-quad-drift) configuration. This approach enables a quasicontinuous distribution of "kick" strength and offers flexibility during the early stage of optimization.

The optimization process employs a multiobjective genetic algorithm based on NSGA-II. The optimization variables include (i) bending angle and radius of the dipoles, (ii) strength of the quadrupoles, and (iii) Courant-Snyder functions at the chosen reference point.

The optimization goals are classified into two groups: (i) linear conditions and (ii) indicators of lattice nonlinearity. The integral $\Gamma = \int \gamma(s) ds$ of the Courant-Snyder gamma function $\gamma$ serves as an indicator for the average path length shift of a particle $[\Delta z \approx -\frac{1}{4}(\epsilon_x \Gamma_x + \epsilon_y \Gamma_y)]$ contributed from betatron oscillation [20] induced by lattice nonlinearity. Including such indicators is beneficial as the linear lattice design forms the foundation for nonlinear optimization. Additionally, pursuing a low value of $\Gamma$ helps avoid cases where the Courant-Snyder functions become excessively large or small or even infeasible.

### B. One specific instance

In this subsection, an example of a linear lattice is presented, comprising 8 dipoles and 38 quadrupoles. The beta and dispersion functions for this specific instance of the GLSF unit are shown in Fig. 14. The linear conditions are fulfilled. It is worth mentioning that this is a demonstration case and can be further optimized if needed.

The realization of $\mathcal{H}_y(\mathrm{Rad}) = 9$ μm in both part 2 and part 3 mir follows the cancellation rules of driving terms

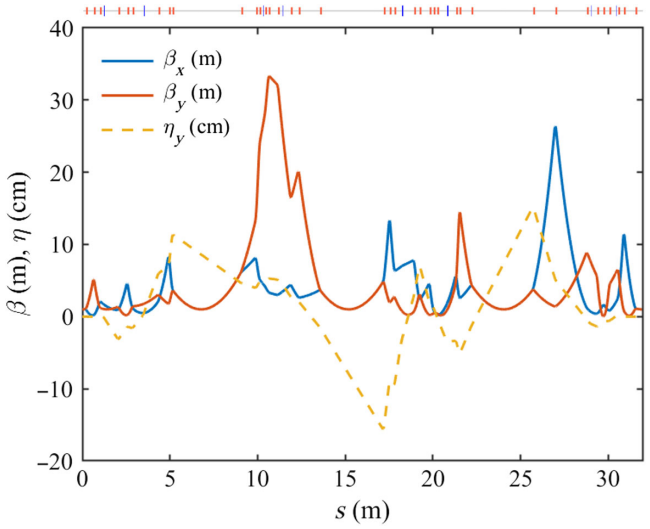


FIG. 14. Beta ($\beta_x$ blue solid, $\beta_y$ orange solid) and dispersion ($\eta_y$ yellow dashed) functions of an instance GLSF unit.

TABLE I. Beam parameters of the launched bunch.

| Parameters | Quantities |
|---|---|
| Horizontal emittance: $\epsilon_x$ | 50 pm rad |
| Vertical emittance: $\epsilon_y$ | 1 pm rad |
| rms bunch length: $\sigma_z$ | 50 nm |
| rms natural energy spread: $\sigma_\delta$ | $2.5 \times 10^{-4}$ |
| Number of particles: $N_{\mathrm{par}}$ | $1 \times 10^4$ |

outlined in Eq. (55). One difference, however, lies in the fact that for part 2, the phase advance of the quadrupole channel between the dipoles is $\psi_{\mathrm{QC}} \to 0$, whereas it is $\psi_{\mathrm{QC}} \to 2\pi$ for part 3 mir. This diversity arises from the opposite signs of $n_{56}$ and $e_{56}$.

This specific instance of the GLSF unit is subsequently tested for "tracking," where the particle coordinates of a launched beam are iterated turn-by-turn. To complete a GLSF storage ring as shown in Fig. 9, a laser modulator Mod0 is placed within the ring. Here Mod0 serves as a prebunching component, which has been explained in Sec. II C. The assumed wavelength of the modulation laser is 1 μm, and a laser power of 150 kW, rather than 1 MW, is sufficient to achieve the desired equilibrium bunch length of 50 nm in the storage ring. It is worth noting that while the wavelength of the modulation laser remains consistent for all three laser modulators, the required laser power for Mod0 is significantly lower compared to Mod1 and Mod2 in the GLSF unit.

The tracking process undertaken here is intended to validate the effectiveness of the concept and linear design of the GLSF unit. Here, linearity is assumed for all lattice components. This implies that the two halves of the storage ring outside the GLSF unit, together with parts 1–4 within the GLSF unit, are represented by their respective linear transfer maps. And for the laser modulators, the manipulation function of Mod0 is sinusoidal $[\Delta\delta = f_0(z) = V_0 \sin(k_{\mathrm{m}} z)]$, while Mod1 and Mod2 $[f_2(z) = -f_1(z)]$ employ both linear $(f_1(z) = hz)$ and sinusoidal $[f_1(z) = V_1 \sin(k_{\mathrm{m}} z)]$ manipulation functions in sequence. The test bunch is launched at the center of Mod0, with initial parameters obtained from the equilibrium beam status

TABLE II. Beam parameters observed at the center of the radiator. The modulation of (Mod1, Mod2) is linear.

| Parameters | Quantities |
|---|---|
| Horizontal rms bunch size: $\sigma_x$ | 7.07 μm |
| Horizontal rms bunch slope: $\sigma_{x'}$ | 7.06 μrad |
| Vertical rms bunch size: $\sigma_y$ | 14.3 μm |
| Vertical rms bunch slope: $\sigma_{y'}$ | 7.35 μrad |
| rms energy spread: $\sigma_\delta$ | $4.79 \times 10^{-4}$ |
| rms bunch length: $\sigma_z$ | 3.03 nm |
| Bunching factor at 13.5 nm: $b$ | 0.372 |

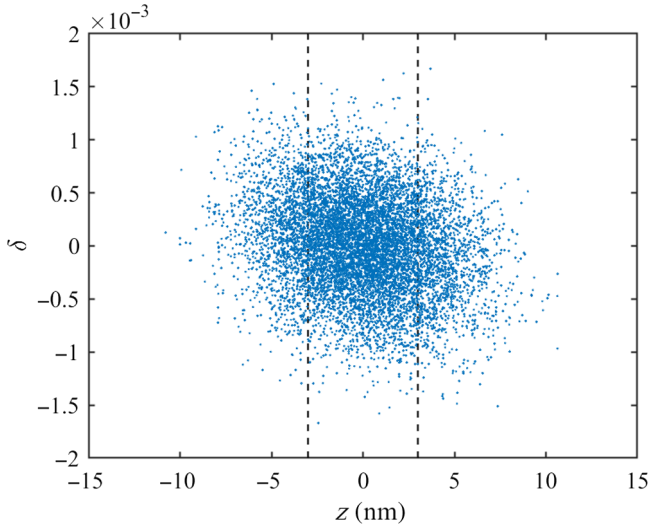


FIG. 15. Beam distribution in the longitudinal phase space observed at the center of the radiator. A linear modulation is applied at (Mod1, Mod2). Dashed lines mark the positions of $z = \pm 3$ nm.

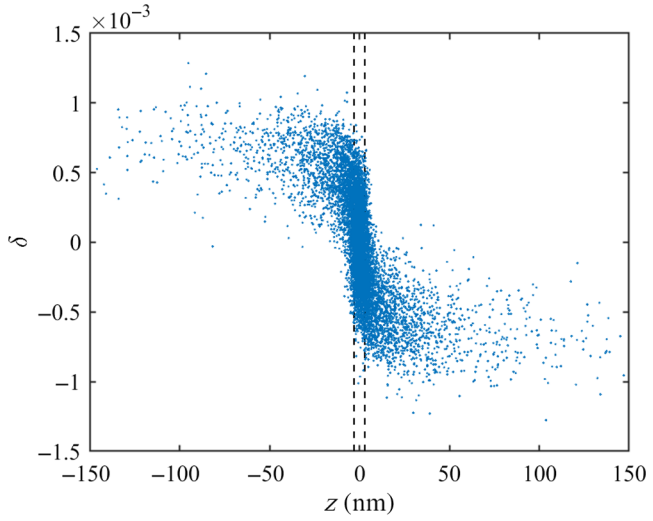


FIG. 16. Beam distribution in the longitudinal phase space observed at the center of the radiator. A sinusoidal modulation is applied at (Mod1, Mod2). Dashed lines mark the positions of $z = \pm 3$ nm.

within an SSMB storage ring (see Table I). The steady-state beam distribution within the GLSF unit can thus be determined in the context of linear beam dynamics. The observation point is positioned at the center of the radiator.

To start with, a linear modulation is applied to Mod1 and Mod2. The observed beam parameters are listed in Table II, and the beam distribution in the longitudinal phase space is depicted in Fig. 15. The obtained results indicate that a steady-state bunch length of 3 nm can be achieved at the radiator in a GLSF SSMB storage ring when employing linear modulations in Mod1 and Mod2. The modulation strength is specified as $|h| = 4000\ \mathrm{m}^{-1}$, and the corresponding power of the modulation laser is 1 MW.

Afterward, a sinusoidal modulation is loaded at Mod1 and Mod2. The observed beam parameters are listed in Table III, and the beam distribution in the longitudinal phase space is depicted in Fig. 16. The nonlinear nature of the sinusoidal modulation introduces distortions to the beam distribution, leading to a reduced bunching factor at the radiator.

TABLE III. Beam parameters observed at the center of the radiator. The modulation of (Mod1, Mod2) is sinusoidal.

| Parameters | Quantities |
|---|---|
| Horizontal rms bunch size: $\sigma_x$ | 7.07 μm |
| Horizontal rms bunch slope: $\sigma_{x'}$ | 7.08 μrad |
| Vertical rms bunch size: $\sigma_y$ | 14.3 μm |
| Vertical rms bunch slope: $\sigma_{y'}$ | 7.27 μrad |
| rms energy spread: $\sigma_\delta$ | $4.14 \times 10^{-4}$ |
| Bunching factor at 13.5 nm: $b$ | 0.153 |

The estimation of the power of the EUV radiation can be determined based on the given parameters below. The beam energy is 400 MeV, and the average beam current is 1 A. The radiator has a period number of 160 and a period length of 1.25 cm. By utilizing the six-dimensional particle coordinates at the center of the radiator, the radiation power at a specific wavelength can be calculated [21]. For a wavelength of 13.5 nm within a ±2% bandwidth, the average radiation power $P_{\mathrm{rad}}$ is determined to be 1.2 kW.

The power of the modulation laser is 1 MW, which is sufficiently low to operate in continuous-wave mode for optical cavities. This indicates that achieving kW-level quasicontinuous-wave 13.5-nm EUV radiation is feasible in a GLSF SSMB storage ring with a modulation laser power in the MW range.

## VI. CONCLUSIONS AND DISCUSSIONS

In this paper, we first introduced the concept of the generalized longitudinal strong focusing (GLSF) scheme. We emphasized its effectiveness in generating ultrashort bunches while simultaneously reducing the demand for modulation laser power. This is accomplished by involving transverse-longitudinal coupling and exploiting the low vertical emittance in a planar storage ring.

Following that, we investigated a bunch compression scheme based on transverse-longitudinal coupling. It was specifically designed for storage rings, serving as an insertion unit to facilitate the bunching and debunching processes on a turn-by-turn basis. We proposed two categories of lattice layouts: symmetric and reversible, with the latter being favored in subsequent designs due to its capability to cancel out the nonlinearity introduced by the modulations.

Additionally, we studied in-depth the linear beam dynamics within the GLSF approach, which includes various aspects such as bunch compression, modulation cancellation, and vertical-longitudinal decoupling. We performed calculations to determine the bunching factor at the radiator, providing evidence to support the claim that the GLSF scheme can effectively reduce the requirement for laser power. Furthermore, we examined the multiple expressions of the $\mathcal{H}$ function and investigated its evolution in magnets.

Finally, we explored the strategies and settings to realize in practice a linear lattice for the GLSF unit. We provided parameters and performance analysis for a specific instance of the linear GLSF lattice. With a beam energy of 400 MeV and an average current of 1 A, we showed that the average radiation power for a wavelength of 13.5 nm within a $\pm 2\%$ bandwidth is 1.2 kW when the power of the modulation laser is 1 MW. This demonstrates the feasibility of achieving kW-level quasicontinuous-wave 13.5-nm EUV radiation in a GLSF SSMB storage ring with MW-level modulation laser power.

We believe that the GLSF scheme can also be applied in conventional storage rings for various purposes related to beam manipulations. For instance, it may provide a novel approach to generate coherent THz radiation and ultrashort pulses.

The analysis of nonlinear dynamics in this paper is in general absent and requires further investigation in future studies. Here is a brief sketch. The nonlinearity of the lattice between the two modulators within the GLSF unit gives rise to a deviation in the longitudinal position of particles from their ideal positions in a perfect linear lattice. This deviation $\Delta z$ can be transformed into $\Delta\delta$ and amplified by the modulations. In contrast to conventional storage rings, the analysis of nonlinear dynamics in GLSF rings incorporates all six dimensions, including the longitudinal dimension $z$. As the longitudinal dynamics play a crucial role in SSMB, a comprehensive optimization of the nonlinear dynamics in all six dimensions is necessary. For laser modulators, their intrinsic momentum compaction leads to distortions in the standard sinusoidal modulation. These distortions behave differently for Mod1 and Mod2 due to their opposite modulation signs. Even with a linear lattice in between, the perfect cancellation of modulations is disrupted, introducing undesired and disturbing transverse-longitudinal coupling. In conclusion, theories and methodologies are much needed to address the challenges posed by nonlinear dynamics in GLSF SSMB storage rings.

Besides optimizing nonlinear beam dynamics, future research could further explore various aspects, including, for instance, the mitigation of timing and phase errors in the modulation laser system, as well as the investigation of coherent synchrotron radiation and other collective effects within the GLSF unit [38–40].

## ACKNOWLEDGMENTS

The authors thank Bocheng Jiang, Cheng-Ying Tsai, Zhenghe Bai, Chao Feng, Yao Zhang, Xing Liu, Lixin Yan, Renkai Li, and Wenhui Huang for helpful discussions. This work is supported by the National Key R&D Program of China (Grant No. 2022YFA1603400), the National Natural Science Foundation of China (NSFC Grant No. 12035010), and the Tsinghua University Initiative Scientific Research Program.

[1] C. Wagner and N. Harned, Lithography gets extreme, Nat. Photonics **4**, 24 (2010).

[2] H. Mizoguchi *et al.*, Update of > 300 W high power LPP-EUV source challenge IV for semiconductor HVM, in *Proceedings of International Conference on Extreme Ultraviolet Lithography 2021*, SPIE Proceedings Vol. 11854 (SPIE-International Society for Optical Engineering, Bellingham, WA, 2021), p. 118540K, http://dx.doi.org/10.1117/12.2600714.

[3] D. F. Ratner and A. W. Chao, Steady-state microbunching in a storage ring for generating coherent radiation, Phys. Rev. Lett. **105**, 154801 (2010).

[4] C. Tang *et al.*, An overview of the progress on SSMB, in *Proceedings of 60th ICFA Advanced Beam Dynamics Workshop, FLS'18, Shanghai, China, 2018* (JACoW, Geneva, 2018), pp. 166–170, http://dx.doi.org/10.18429/JACoW-FLS2018-THP2WB02.

[5] X. Deng *et al.*, Experimental demonstration of the mechanism of steady-state microbunching, Nature (London) **590**, 576 (2021).

[6] D. Ratner and A. Chao, Reversible seeding in storage rings, in *Proceedings of 33rd International Free Electron Laser Conference (FEL'11), Shanghai, China, 2011* (JACoW, Geneva, 2011), pp. 57–60, http://jacow.org/fel2011/papers/mopb23.pdf.

[7] A. Chao, E. Granados, X. Huang, H. Luo, and D. Ratner, High power radiation sources using the steady-state microbunching mechanism, in *Proceedings of 7th International Particle Accelerator Conference, IPAC'16, Busan, Korea, 2016* (JACoW, Geneva, 2016), pp. 1048–1053, http://dx.doi.org/10.18429/JACoW-IPAC2016-TUXB01.

[8] C. Tang and X. Deng, Steady-state micro-bunching accelerator light source, Acta Phys. Sin. **71**, 152901 (2022).

[9] X. J. Deng, A. W. Chao, J. Feikes, W. H. Huang, M. Ries, and C. X. Tang, Single-particle dynamics of microbunching, Phys. Rev. Accel. Beams **23**, 044002 (2020).

[10] Z. Pan, A. Chao, X. Deng, W. Huang, T. Rui, C. Tang, W. Wan, and Y. Zhang, A storage ring design for steady-state microbunching to generate coherent EUV light source, in *Proceedings of 39th International Free Electron Laser Conference, FEL'19, Hamburg, Germany, 2019* (JACoW, Geneva, 2019), pp. 700–703, http://dx.doi.org/10.18429/JACoW-FEL2019-THP055.

[11] Y. Zhang, X. J. Deng, Z. L. Pan, Z. Z. Li, K. S. Zhou, W. H. Huang, R. K. Li, C. X. Tang, and A. W. Chao, Ultralow longitudinal emittance storage rings, Phys. Rev. Accel. Beams **24**, 090701 (2021).

[12] D. Xiang and W. Wan, Generating ultrashort coherent soft x-ray radiation in storage rings using angular-modulated electron beams, Phys. Rev. Lett. **104**, 084803 (2010).

[13] C. Feng, H. Deng, D. Wang, and Z. Zhao, Phase-merging enhanced harmonic generation free-electron laser, New J. Phys. **16**, 043021 (2014).

[14] C. Feng and Z. Zhao, A storage ring based free-electron laser for generating ultrashort coherent EUV and x-ray radiation, Sci. Rep. **7**, 4724 (2017).

[15] M. Sands, The physics of electron storage rings: An introduction, SLAC, CA, Technical Report No. 121, 1970, https://doi.org/10.2172/4064201.

[16] Y. Shoji, H. Tanaka, M. Takao, and K. Soutome, Longitudinal radiation excitation in an electron storage ring, Phys. Rev. E **54**, R4556 (1996).

[17] X. J. Deng, A. W. Chao, W. H. Huang, and C. X. Tang, Courant-Snyder formalism of longitudinal dynamics, Phys. Rev. Accel. Beams **24**, 094001 (2021).

[18] X. J. Deng, A. W. Chao, J. Feikes, A. Hoehl, W. H. Huang, R. Klein, A. Kruschinski, J. Li, M. Ries, and C. X. Tang, Breakdown of classical bunch length and energy spread formula in a quasi-isochronous electron storage ring, Phys. Rev. Accel. Beams **26**, 054001 (2023).

[19] Z. Pan, Research on optimization and design of advanced laser-driving storage ring, Ph.D. thesis, Tsinghua University, Beijing, China, 2020.

[20] A. Chao, *Lectures on Accelerator Physics* (World Scientific, Singapore, 2020), https://doi.org/10.1142/12004.

[21] Y. Zhang, Research on longitudinal strong focusing SSMB ring, Ph.D. thesis, Tsinghua University, Beijing, China, 2022.

[22] M. Cornacchia and P. Emma, Transverse to longitudinal emittance exchange, Phys. Rev. ST Accel. Beams **5**, 084001 (2002).

[23] P. Emma, Z. Huang, K. J. Kim, and P. Piot, Transverse-to-longitudinal emittance exchange to improve performance of high-gain free-electron lasers, Phys. Rev. ST Accel. Beams **9**, 100702 (2006).

[24] B. Jiang, J. G. Power, R. Lindberg, W. Liu, and W. Gai, Emittance-exchange-based high harmonic generation scheme for a short-wavelength free electron laser, Phys. Rev. Lett. **106**, 114801 (2011).

[25] C. Feng, T. Zhang, H. Deng, and Z. Zhao, Three-dimensional manipulation of electron beam phase space for seeding soft x-ray free-electron lasers, Phys. Rev. ST Accel. Beams **17**, 070701 (2014).

[26] X. Wang, C. Feng, T. Liu, Z. Zhang, C. Tsai, J. Wu, C. Yang, and Z. Zhao, Angular dispersion enhanced prebunch for seeding ultrashort and coherent EUV and soft X-ray free-electron laser in storage rings, J. Synchrotron Radiat. **26**, 677 (2019).

[27] X. Wang, C. Feng, C. Y. Tsai, L. Zeng, and Z. Zhao, Obliquely incident laser and electron beam interaction in an undulator, Phys. Rev. Accel. Beams **22**, 070701 (2019).

[28] X. Wang, C. Feng, C. Yang, L. Zeng, and Z. Zhao, Transverse-to-longitudinal emittance-exchange in optical wavelength, New J. Phys. **22**, 063034 (2020).

[29] Y. Lu, X. Wang, X. Deng, C. Feng, and D. Wang, Methods for enhancing the steady-state microbunching in storage rings, Results Phys. **40**, 105849 (2022).

[30] X. Deng, W. Huang, Z. Li, and C. Tang, Harmonic generation and bunch compression based on transverse-longitudinal coupling, Nucl. Instrum. Methods Phys. Res., Sect. A **1019**, 165859 (2021).

[31] H. Deng and C. Feng, Using off-resonance laser modulation for beam-energy-spread cooling in generation of short-wavelength radiation, Phys. Rev. Lett. **111**, 084801 (2013).

[32] G. Wang, W. Zhang, X. Yang, C. Feng, and H. Deng, Fully coherent hard X-ray generation by two-stage phase-merging enhanced harmonic generation, Chin. Phys. C **40**, 098101 (2016).

[33] Z. Zhao, H. Li, and Q. Jia, Phase-merging enhanced harmonic generation free-electron laser with a normal modulator, J. Synchrotron Radiat. **24**, 906 (2017).

[34] C. Li, C. Feng, and B. Jiang, Extremely bright coherent synchrotron radiation production in a diffraction-limited storage ring using an angular dispersion-induced microbunching scheme, Phys. Rev. Accel. Beams **23**, 110701 (2020).

[35] C. Li, B. Jiang, C. Feng, D. Huang, Q. Zhang, and K. Wang, Lattice design for angular dispersion enhanced microbunching in storage rings, J. Instrum. **16**, P03004 (2021).

[36] B. Jiang *et al.*, A synchrotron-based kilowatt-level radiation source for EUV lithography, Sci. Rep. **12**, 3325 (2022).

[37] Y. Shoji, Bunch lengthening by a betatron motion in quasi-isochronous storage rings, Phys. Rev. ST Accel. Beams **7**, 090703 (2004).

[38] C. Y. Tsai, A. W. Chao, Y. Jiao, H. W. Luo, M. Ying, and Q. Zhou, Coherent-radiation-induced longitudinal single-pass beam breakup instability of a steady-state microbunch train in an undulator, Phys. Rev. Accel. Beams **24**, 114401 (2021).

[39] C.-Y. Tsai, Theoretical formulation of multiturn collective dynamics in a laser cavity modulator with comparison to Robinson and high-gain free-electron laser instability, Phys. Rev. Accel. Beams **25**, 064401 (2022).

[40] C.-Y. Tsai and X. Deng, A recursive model for laser-electron-radiation interaction in insertion section of SSMB storage ring based on transverse-longitudinal coupling scheme, in *Proceedings of 67th ICFA Advanced Beam Dynamics Workshop on Future Light Sources FLS2023, Luzern, Switzerland, 2023* (JACoW, Geneva, 2023), http://fls2023.vrws.de/papers/tu4p31.pdf.